Astrocytic glutamate regulation is implicated in the development of stress-related psychiatric disorders

Dominic Kaul[1,2], Amber R Curry[1,2], Nathalie Gerstner[3,4,5], Anna S Fröhlich[3,4], Caine C Smith[1], Greg T Sutherland[1], Mirella Dottori[6], Michael J Ziller[3,7], Elisabeth B Binder[3], Janine Knauer-Arloth[3,5], Naguib Mechawar[8], Sibylle G Schwab[6], Lezanne Ooi[2], Natalie Matosin[1,2*]

[1]School of Medical Sciences, Faculty of Medicine and Health, University of Sydney, Sydney, New South Wales, Australia
[2]School of Chemistry and Molecular Bioscience and Molecular Horizons, University of Wollongong, Wollongong, New South Wales, Australia
[2]Department of Genes and Environment, Max Planck Institute of Psychiatry, Kraepelinstr. 2-10, 80804, Munich, Germany
[3]International Max Planck Research School for Translational Psychiatry, Kraepelinstr. 2-10, 80804, Munich, Germany
[4]Institute of Computational Biology, Helmholtz Zentrum München, Ingolstaedter Landstr. 1, 85764, Neuherberg, Germany
[5]Department of Psychiatry, University of Münster, Münster, Germany
[6]Douglas Institute, Department of Psychiatry, McGill University, Montreal, QC, Canada
[7]School of Medical Indigenous and Health Sciences, Molecular Horizons, University of Wollongong, NSW 2522, Australia

Severe psychological stress is one of the most potent risk factors for developing a mood or psychotic disorder, yet the underlying molecular mechanisms are poorly understood. Astrocytes are a key brain cell type associated with stress and psychiatric phenotypes in animals, but how this translates to humans is largely unknown. Here, we show that cortical astrocytes are persistently changed both physically and molecularly in humans with psychiatric disorders exposed to profound stress before diagnosis. By profiling the diversity of human astrocytes with single nucleus and spatial transcriptomics, we identified distinct alterations to glutamate-related synaptic functions, supported by histological quantification of >20,000 astrocytes. Alterations were pronounced in females compared to males and in cases exposed to profound stress during childhood. The use of human pluripotent stem cell-derived astrocytes confirmed that glutamate signalling is directly impacted by glucocorticoid activation. Our findings suggest that astrocytes are strategic pharmacological targets for future intervention strategies.

Severe psychological stress is a global issue. The accumulation of recent geopolitical, environmental, and health crises has highlighted that stress has broad and substantial ramifications for mental health. For example, in the first year of the COVID-19 pandemic, the worldwide incidence of depression and anxiety increased by 25%[1]. It is also estimated that at least one in two children is impacted by maltreatment, a key psychological stressor globally[2]. These exposures are robust risk factors for a plethora of medical conditions, including psychiatric disorders[3,4], and are often associated with impaired treatment responsiveness[5,6] and increased symptom severity[7-9]. Consequently, there is strong evidence that severe stress causes clinically relevant biological contributions to mental health disorders. However, understanding how these findings translate to human populations has been challenging given the complexity associated with defining what constitutes impactful 'stress' and associating this with clinical consequences, such as diagnosis. Recent approaches to pinpoint underlying molecular signatures have highlighted that both cell-type[10,11] and spatial domains[12] of the prefrontal cortex (PFC) are essential to shaping the brain in response to stress, with astrocytes emerging as a focus across stress-related psychiatric disorders[10,13,14]. Cerebral astrocytes are highly abundant and play essential roles across many brain functions, especially in coordinating the synaptic, metabolic, and neuroinflammatory environments[15]. Astrocytes directly contact blood vessels, positioning them as key responders to circulating signalling molecules passing the blood-brain barrier, including cortisol[16]. Importantly, astrocytes represent a molecularly and regionally diverse population of cells that has relevance to health and pathologies[13,16-19]. Taking into account this diversity is crucial to understanding complex conditions, such as stress-associated psychiatric disorders in the human brain, where specialised functions, such as astrocyte-mediated cholesterol synthesis, have been previously implicated[13].

In this study, we utilised a range of high-resolution techniques, including single nucleus RNA sequencing (snRNAseq) from the post-mortem prefrontal cortex (PFC) of 87 individuals and spatial transcriptomics from 13 of these individuals, as well as morphometric analysis of more than 20,000 astrocytes to explore the molecular and spatial diversity of astrocytes in this neocortical area. We then examined this cohort to identify how cases of psychopathologies with a well-defined, profound clinical history of stress before diagnosis vary from those without to dissect lasting alterations to astrocytes associated with significant psychological stress and explore the importance of sex

and timing of stress exposure. We also demonstrate that core functions of astrocytes that regulate glutamate neurotransmission are responsive to the activation of cortisol receptors by employing human pluripotent stem cell (hPSC)-derived astrocytes. Together, transcriptomic, morphological, and *in vitro* evidence converge to show that human astrocytes persistently change after stress. This has the potential to benefit treatment specificity as well as the development and implementation of early intervention and prevention strategies for psychiatric disorders related to severe stress exposure.

Results

SnRNAseq identifies transcriptional diversity of astrocytes in the human orbitofrontal cortex

We analysed the orbitofrontal cortex (OFC; Brodmann Area 11), a region important to emotion-related learning and perceiving stress[20]. It is also implicated across psychiatric disorders[21,22] and thus provides unique insight into the intersection of stress and psychiatry (Figure 1; demographics outlined in Supplementary Figure 1). To first examine the transcriptional heterogeneity of human cortical astrocytes, we used snRNAseq from the OFC of 32 controls not diagnosed with a psychiatric disorder and 55 individuals diagnosed with a psychiatric disorder (major depression, bipolar disorder, schizoaffective disorder, or schizophrenia). Clustering of 111,516 astrocytes identified 10 well-distributed clusters (Figure 2a, Supplementary Figure 2d-f). Several of these clusters were in common with a prior integration of 17 human snRNAseq datasets across 302 individuals[23]. This included a cluster enriched for amyloid metabolism (*APOE* and *CLU*; cluster 1), 'pan-reactive'-like astrocytes (*GFAP*, *VIM*, *NEAT1*; cluster 8), and phagocytotic astrocytes (*ELMO1*, *MEF2A*; cluster 9) (Figure 2b). Cluster 6 also expressed markers of interlaminar astrocytes, including *ID3*, *SERPINI2*, and *WDR49* (among the top 100 most enriched genes, Supplementary Data S1)[13,24]. Clusters were robustly delineated by broad cell type label annotation as either protoplasmic (clusters 0,1,2,3,5 composed 88% of the protoplasmic label) or fibrous (clusters 4,6,7 composed 98% of the fibrous label) except for reactive cluster 8, which was identified in both low-resolution annotations (84% protoplasmic, 16% fibrous; Supplementary Figure 3a). Correlation between clusters further supported these cell type annotations, with fibrous clusters (4 and 6), protoplasmic clusters (0-5), and reactive-like astrocytes (8-9) forming distinct clades (Supplementary Figure 3b).

To explore whether these transcriptionally defined populations of astrocytes were associated with functional niches beyond low-resolution labels (i.e. protoplasmic/fibrous), we performed gene set enrichment analysis (GSEA) across the entire transcriptome of each cluster using Molecular Function, Biological Processes, and Cellular Compartment gene ontology sets. This approach highlighted key functions, including astrocyte populations enriched for transcripts regulating synaptic activity and gliotransmission (clusters 0 and 5; e.g. synapse organisation and exocytosis, reflective of clusters identified previously[18]), neurotransmitter and metabolic homeostasis (clusters 1, and 2 ; e.g. neurotransmitter reuptake) or immune response (cluster 8 and 9; e.g. cytokine signalling, and phagocytosis) (Figure 2c). There were also unique terms that further delineated clusters. For example, cluster 5 was enriched for glutamate and γ-aminobutyric acid (GABA) signalling, and cluster 1 was enriched for aerobic respiration. We also identified that cluster 7, which was poorly defined at a marker level, with expression of both grey matter markers (*SLC1A2*) and white matter markers (*DPP10*), was uniquely enriched for functions related to water and gas transport. It also expressed *GFAP* and the water channel *AQP4*, and thus may be reflective of varicose projection astrocytes, a substate of deeper layer/white matter astrocytes[25]. Functional terms enriched across the clusters were disproportionately associated with regulating the neuronal environment and neurotransmitter transport (59% of terms), supporting prior evidence that the surrounding cellular and synaptic environment is an important driver of astrocyte diversity (Supplementary Figure 3c-d, Supplementary Data S2)[26,27].

Spatial transcriptomics confirms astrocyte diversity of OFC astrocytes

Given previous evidence that astrocytes demonstrate functionally relevant laminar distributions in the cortex[26-28], we also sought to determine whether we could detect laminar populations of astrocytes. To synthesise a transcriptional reference for these layers, we performed spatial transcriptomics (Visium, 10x Genomics) in a subset of individuals from this cohort (n=13, full demographics available in Supplementary Figure 1). After quality control, integration, and clustering, we delineated six spatial domains across all 13 individuals (layers II, III, IV, V, VI, and white matter; Figure 2d). Clustering did not associate with covariates (Age, Sex, PMI, Batch), and domains were consistent between individuals when domains were

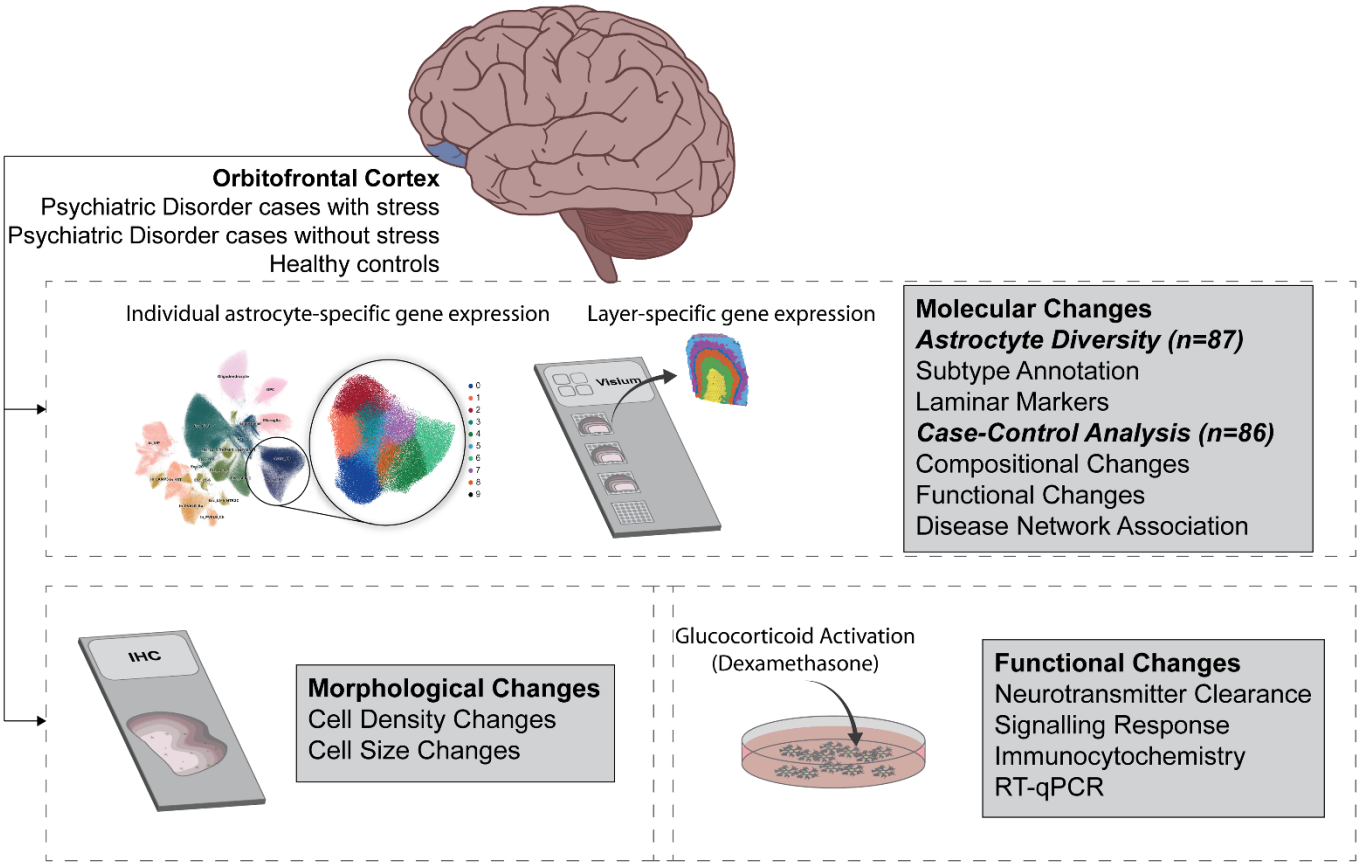

Figure 1: Schematic of experimental workflow. Profound stress history and diagnosis of history of severe psychiatric disorder were extracted from a postmortem cohort of 92 individuals. Tissue sections from the 3rd ~1cm coronal slice of Brodmann are 11 were acquired. Nuclei were extracted, processed, sequenced, integrated, and then labelled by cell type, consisting of 87 libraries which met quality control thresholds. Additional sections were mounted onto Visium slides for spatial transcriptomics in a subset of these 87 libraries. Immunohistochemistry in a largely overlapping subset of this cohort was used to validate spatially annotated astrocyte populations associated with a history of profound stress. Glucocorticoid activation of astrocytes was used to determine alterations to the functions of human astrocytes to coordinate the synapse.

remapped onto individual slides *in situ* (Supplementary Figure 4). Layer markers were then corroborated with prior spatial transcriptomics datasets that manually annotated layers based on histology (layer I: *RELN*, layer II: *CALB1*, layer III: *NEFL*, layer IV: *RORB*, layer V: *PCP4*, layer 5: *DIRAS2*, white matter: *MBP*; Figure 2e, top 100 genes per layer are provided in Supplementary Data S3)[29,30]. We also performed gene ontology analysis on the top 100 genes from each layer using EnrichR, which further supported layer identities, highlighting domains enriched for relevant functions (e.g. white matter: myelination, layer V: signal release from synapse, layer III: GABAergic synaptic transmission, Supplementary Data S4). Together, this semi-automated integration method identified conserved histologically relevant domains across the human OFC.

We then used the machine learning tool Tangram[31] to spatially locate cells based on the most probable spatial transcriptomic domain. This efficiently identified the enrichment of expected populations, such as layer II-III and layer IV-VI excitatory neurons in their corresponding cortical layers and oligodendrocytes in the white matter (Figure 2f). Given the propensity of snRNAseq deconvolution approaches to assign astrocytes to layer I or white matter[32,33], targeted approaches are necessary to integrate the two platforms at higher resolutions. We employed the cluster mode to predict the probability of each cell occurring at each broadly annotated layer. In support of this approach, 65% of astrocytes assigned to the white matter were derived from fibrous clusters 4, 6, and 7, while predicted protoplasmic clusters 0 and 5, associated with synaptic regulation, were most frequently assigned to the neuronal layers III and V (86.1%, 23.6% of these layers, respectively). Cluster 2, involved in neurotransmitter homeostatic functions, was enriched in layer IV (36.2% of astrocytes in this layer), a primary input layer of the cortex. We also wanted to discern whether specific molecular markers delineated these laminar astrocyte populations. This identified enriched ($P_{adj}<0.05$) genes, including semaphorin 3A (*SEMA3A*) in layer VI and the potassium voltage-gated channel subunit *KCNB2* in layer III (Figure 2g; Supplementary Data S5). However, it is important to note that only 56% of astrocytes met the applied 1.5-fold enrichment threshold, suggesting that transcriptionally distinct laminar populations, at

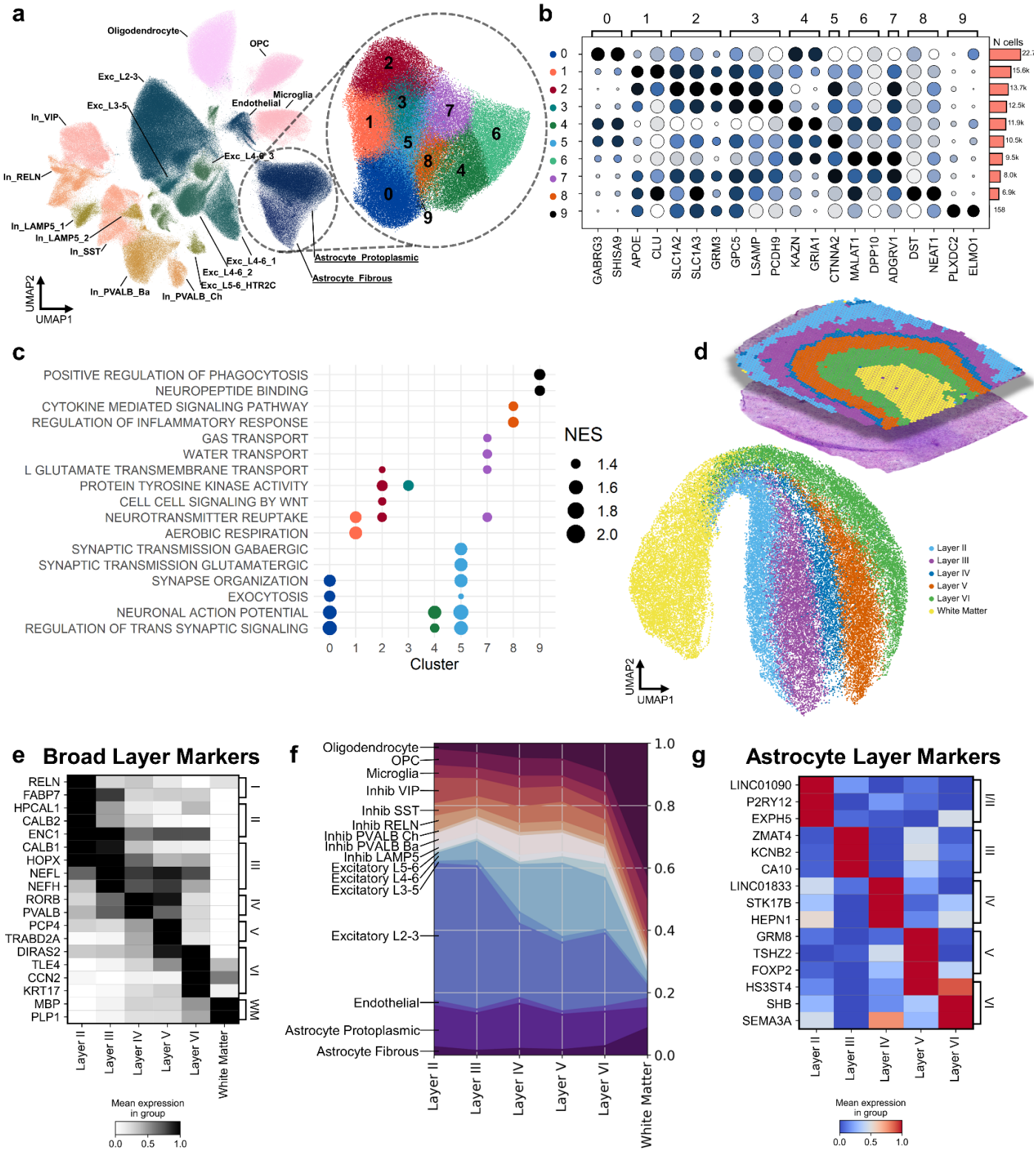

Figure 2: Characterisation of human astrocytes in the orbitofrontal cortex highlights functional and regional heterogeneity (a) UMAP representation of single nucleus RNA sequencing from >800,000 cells and reclustered astrocytes (in zoom) coloured by cluster as determined by Leiden algorithm (b) Dotplot of markers of each astrocyte cluster from snRNAseq analysis. Spot darkness indicates scaled mean gene expression across clusters and spot size indicates proportion of nuclei in cluster above single cell transformed expression cutoff > 0.5. (c) Gene set enrichment analysis using the C5 biological processes dataset by cluster. Ranks were taken as the score (rank_gene_markers, method = Wilcoxon). Terms were pruned for semantic similarity using the GO.db to keep most significant child terms. Dots indicate significant enrichment per cluster (PFDR < 0.05), dot size indicates normalised enrichment score, and spot colour indicates cluster. (d) UMAP representation of spatial transcriptomics (Visium) dataset from 13 individuals consisting of ~50,000 spatial points. Integration and clustering between individuals were performed using STAligner and mclust pipelines (upper). Datapoints from integrated dataset were mapped onto individual slides to confirm regional identities (lower). (e) General layer markers from spatial transcriptomics curated using rank_genes_groups and from manually annotated datasets. Darkness indicates mean expression in group, scaled per gene. (f) Integration of the complete snRNAseq dataset with the complete spatial transcriptomics dataset using Tangram. Colours represent the proportion of each cell type at each layer of the cortex. (g) Layer markers for astrocytes. Markers determined using pseudobulk approach. Cells were defined to layers using the Tangram tool (>1.5-fold change confidence), and pseudobulk counts per individual were used to determine candidate layer markers. Colour indicates mean expression in group, scaled per gene.

least with this method applied to the present cohort, are relatively conservative. Together, these approaches demonstrate that astrocytes exhibit are transcriptionally diverse in the human cortex and that spatial localisation and cell state are drivers of this.

Profound stress delineates cluster-specific transcriptomic changes in grey matter astrocytes

Next, we sought to utilise this cohort to identify molecular markers delineating individuals with psychiatric disorders exposed to profound psychological stress before diagnosis (3 bipolar disorder/4 major depression/2 schizoaffective disorder/15 schizophrenia) compared to those without (2 bipolar disorder/2 major depression/5 schizoaffective disorder/23 schizophrenia), as well as to compare these to individuals not diagnosed with a psychiatric disorder. First, we investigated whether there were compositional changes to astrocyte clusters between stress-stratified cases. We retrained the Tangram approach as above using the snRNAseq and spatial transcriptomics data derived from each stratified group to predict the composition of astrocyte populations across spatial domains. In the cases with profound stress (Figure 3c), the composition of astrocytes assigned to each layer varied from both controls (Figure 3a) and the cases without profound stress (Figure 3b). Most notably, there was an 18.8% increase in protoplasmic cluster 0 in layer VI and 9.9% increase in cluster 2 in layer IV. In support of this effect, in the snRNAseq dataset, there was a nominal decrease in the proportion of protoplasmic astrocytes across broad cell types (P=0.023), as well as

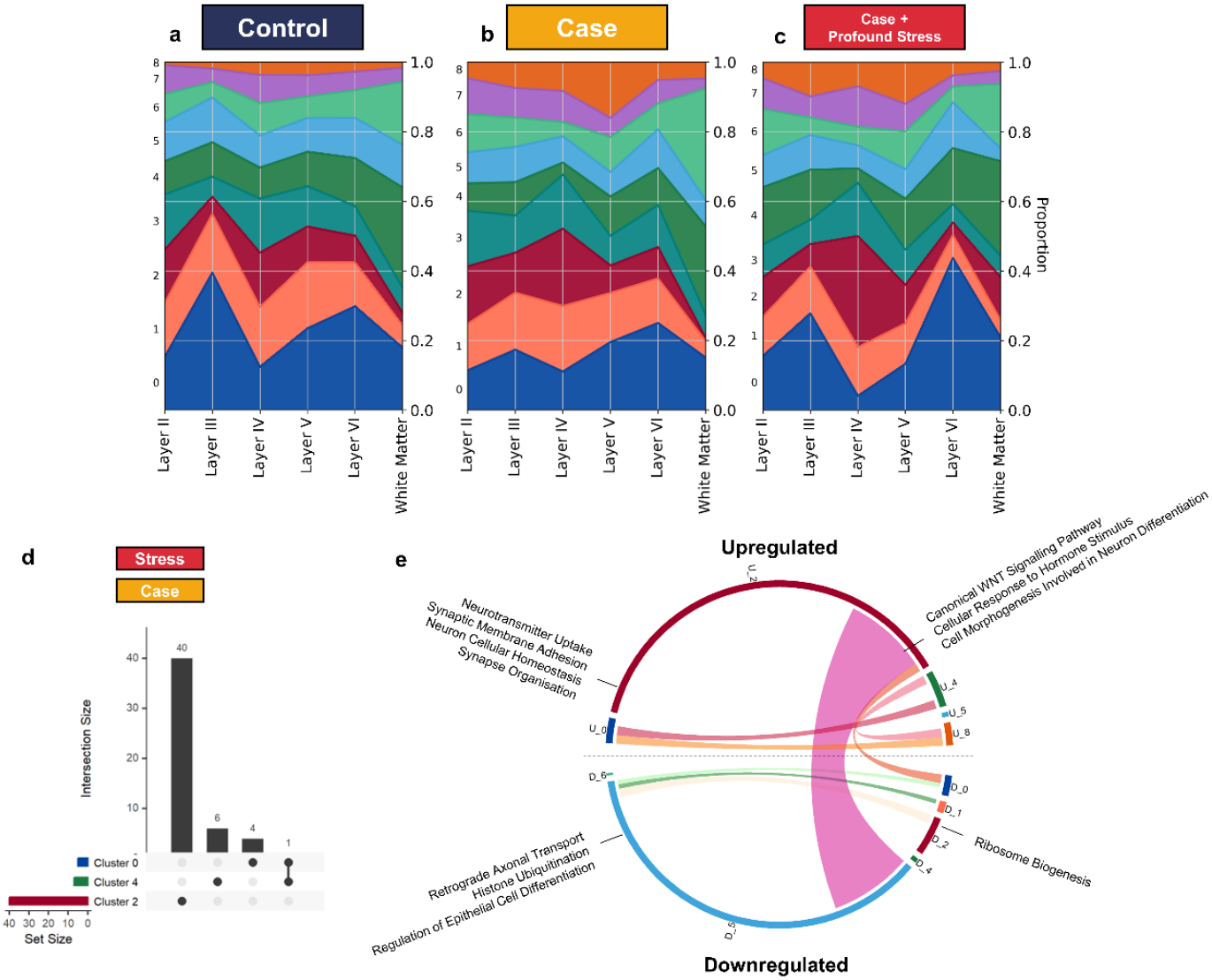

Figure 3: Cortical astrocyte diversity delineates cases of psychiatric disorders with a profound history of stress. (a) Integration of the complete snRNAseq dataset with the complete spatial transcriptomics dataset representing the proportion of each cell type at each layer of the cortex. (b-d) Integration of snRNA astrocyte-specific dataset with spatial transcriptomics from stress delineated groups. Datasets were integrated using the Tangram clusters mode to predict cell likelihood at each laminar distribution. (e) UpSet plot depicting the differentially expressed genes between profound stress and remaining cases (PFDR<0.1). Set size indicates number of genes meeting threshold for each cluster and dots connected by a line indicate common genes. (f) Chord diagram of gene set enrichment analysis performed on differentially expressed gene lists per cluster. Size of arc denotes number of significant terms (PFDR<0.05) and ribbons denote common terms. GO Terms delineated based on positive (U_) or negative (D_) enrichment in cluster. Candidate functional terms annotated following pruning for semantic similarity.

a nominally significant increase within astrocyte cluster 2 (P=0.012) between cases and controls and a decrease between the stress-stratified cases in cluster 1 (P=0.045), although these did not survive correcting for multiple testing (P_{adj}>0.05; Supplementary Figure 5).

To capture transcriptomic changes associated with a profound history of stress, we first performed differential expression analysis between the individuals diagnosed with a psychiatric disorder stratified by stress (no stress vs stress). The most differentially expressed genes (DEGs) were identified in the homeostatic cluster 2 (40 DEGs; 33 upregulated), including increased expression of the nuclear receptor *RORA*, previously associated with childhood abuse in cases of post-traumatic stress disorder[34] and Limbic System Associated Membrane Protein (*LSAMP*), which has been identified to be increased in the synaptosome of the OFC in postmortem individuals with schizophrenia[35] (Figure 3d, Supplementary Data S6). Only a single gene, the cation channel *TRPM3*, was implicated in more than one cluster (downregulated in clusters 0 and 4, Figure 3d). We also identified that DEGs between cases and controls not diagnosed with a psychiatric disorder were broadly consistent regardless of the stress-stratified group used. These effects were similarly most pronounced in the homeostatic clusters 2, 3, and 7 (Supplementary Data S7). To support whether DEGs associated with profound stress were relevant to psychiatric disorders, we used the EnrichR tool to assess gene-disease association via DisGenNET. Several major psychiatric disorders were significantly associated with DEGs, including bipolar disorder (P_{adj}=3.8x10^{-5}, odds ratio=7.94), major depression (P_{adj}=1.4x10^{-4}, odds ratio=9.35), and schizophrenia (P_{adj}=1.4x10^{-4}, odds ratio=5.17).

We then used GSEA as applied in recent analyses of psychiatric human postmortem cohorts[10,14] to determine functional annotations associated with stress stratification within each cluster. This approach also highlighted that clusters 2 and 5 disproportionately contributed to significantly enriched functions (e.g. 146 and 125 terms P_{FDR}<0.05 in the biological processes database, respectively). Uniquely altered functions in cluster 2 were associated with increased neuron homeostatic functions and synaptic remodelling (e.g. neurotransmitter uptake, synaptic membrane adhesion, and dendrite development). In contrast, those in cluster 5 were associated with reduced histone ubiquitination and cellular differentiation (Figure 3e). We also noted a moderate overlap in significant functions between cluster 2 and cluster 5 for example, WNT signalling and hormone stimulus, although these exclusively occurred in opposite directions (up in cluster 2, down in cluster 5).

Females with psychiatric disorders with prior profound stress demonstrate more pronounced astrocyte-specific gene expression changes

Sex has a robust role in the aetiology of psychiatric disorders. Transcriptomic profiling across multiple psychiatric disorders demonstrates notable transcriptomic differences in the PFC of males and females[36,37], which are relevant at the single-cell resolution in the DLPFC of these disorders[14]. To explore these effects in the present study, we reperformed differential expression analysis on males and females individually (55 males, 32 females; Figure 4a). Between the stress-stratified cases, autosomal DEGs were almost exclusively observed in the female clusters (98%), and not correcting for sex increased the number of DEGs detected. These female-specific DEGs reflected the DEGs before stratification by sex, with striking differences, particularly in metabolic cluster 2 (increasing from 40 to 94 DEGs) and homeostatic cluster 3 (increasing from 0 to 351 DEGs; Figure 4a). Using DisGenNET Database to determine disease associations with the whole list of DEGs, schizophrenia was again over-represented as the top hit (P_{adj} =1.92x10^{-4}, odds ratio = 2.1); the most represented diagnosis in the present study. To further support sex-biased effects, we performed rank-rank hypergeometric overlap between male and female DEGs associated with stress-stratified cases. This demonstrated a weak concordance in sex-specific overlap at both low-resolution (protoplasmic/fibrous) and high-resolution (cluster) levels (Figure 4b; Supplementary Figure 7). Reflective of prior bulk transcriptome studies[36], case-control DEGs demonstrated strongly discordant expression patterns between males and females at both low and high resolutions (Figure 4b). For males and females, cluster 2 and 3 contributed almost all DEGs in case-control comparisons (Supplementary Figure 8). Stratifying by sex also abolished divergently enriched functions between clusters within stress-stratified cases and highlighted there were substantially more altered functional terms in females, with more connectedness between groups. This was most evident between clusters 2, 3 and 7, which shared a substantial overlap in enriched functions (Figure 4c). These overlaps were consistent with analysis performed after batch correcting for sex, including enrichment cell-cell adhesion and neurotransmitter uptake. Further, these DEGs were disproportionately associated with human

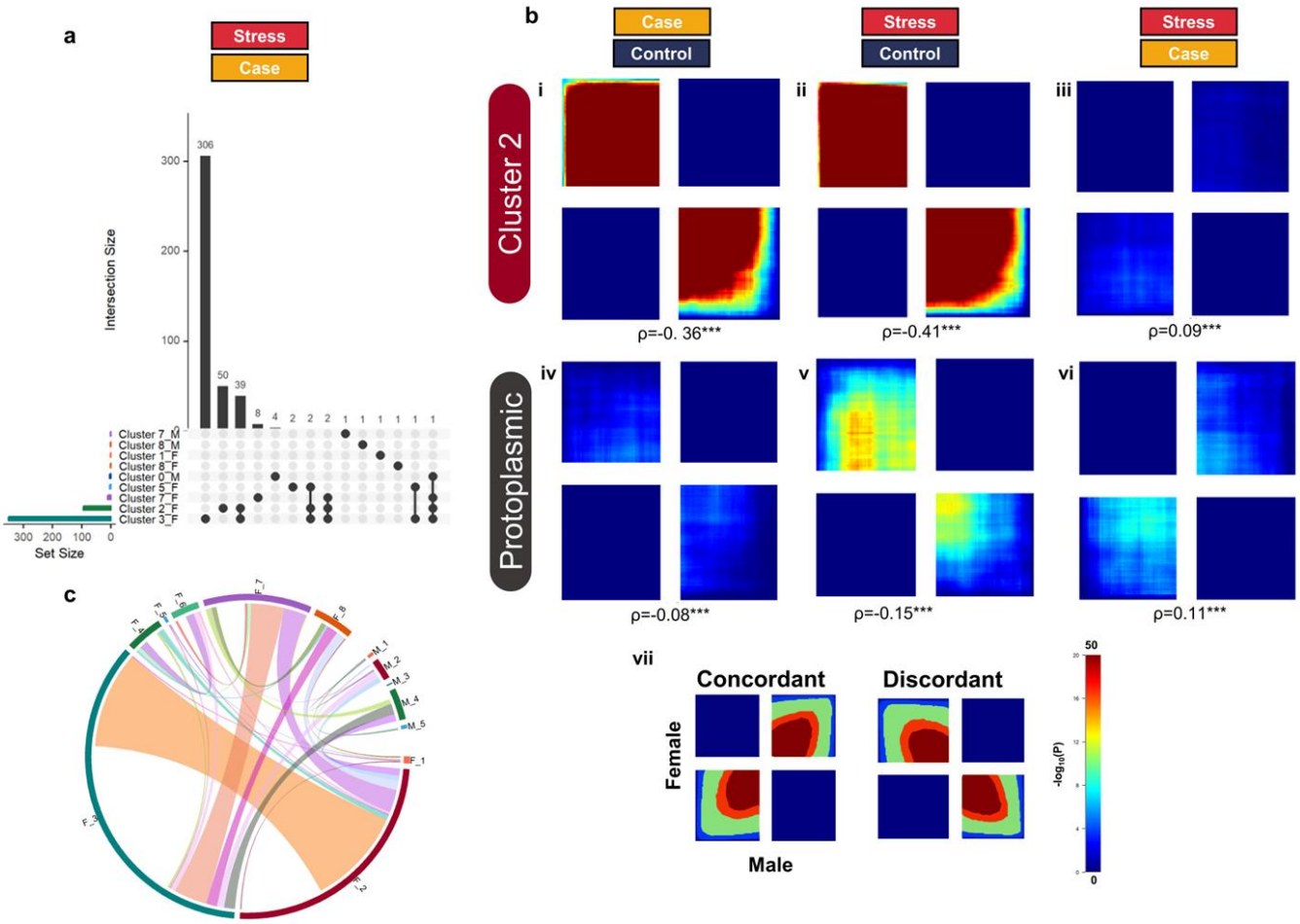

Figure 4: Sex demonstrates discordant case-control effects in homeostatic astrocytes, females demonstrate stronger transcriptomic associations with stress stratification. (a) UpSet plot depicting the differentially expressed genes between 'high' and 'low' stress cases (PFDR<0.1). Set size indicates number of genes meeting threshold for each cluster and dots connected by a line indicate common genes. F indicates data derived from females. (b) Rank-rank hypergeometric overlap between differentially expressed genes stratified by sex. Panel i-iii denote cluster 2 comparisons, iv-vi denote broad protoplasmic comparisons, panel vii denotes shared dimensions, including scale range, explanation of quadrants and axes (c) Chord diagram of gene set enrichment analysis performed on differentially expressed gene lists per cluster by sex. Size of arc denotes number of significant terms (PFDR<0.05) and ribbons denote common terms. GO Terms delineated based on male (M_) or female (F_).

grey matter astrocyte genes (P_{adj}=7.1x10^{-11}, odds ratio =21.75 Allen Brain Atlas 10x scRNA 2021). These results indicate that female cases of psychiatric disorders demonstrate stronger associations with prior profound stress within the context of astrocytes. Additionally, grey matter astrocytes involved in homeostatic functions disproportionately associate with both diagnosis and stress history within diagnoses.

Timing of profound stress exposure associates with transcriptomic and morphological changes to astrocytes

Given that early life stress disproportionately contributes to psychiatric disorder risk[38], we were also interested in whether the timing of exposure influenced gene expression. We delineated the cohort based on the timing of the first profound, severe psychological stress (childhood (<12, n=6), 4: adolescence (12-18, n=6), early adulthood (18-25, n=5), adulthood (>25,n=7) and no profound stress. In total, five genes in cluster 2 and two in cluster 3 were significantly associated with stress timing (P_{adj}<0.1), including DEGs overlapping with analysis of all profoundly stressed individuals. These were particularly related to synapse adhesion (e.g. *LSAMP*, *CADM2*; Figure 5a/b).

To further support these findings, we quantified the morphology and density of astrocytes expressing the glutamate transporter EAAT2 (encoded by *SLC1A2*) using immunohistochemistry on whole coronal sections from a subset of this cohort (Figure 5c/d, cohort outlined in Supplementary Figure 3). We have previously used this subset to explore the contribution of profound adulthood and childhood stress to psychopathologies[39]. We quantified the morphology of 21,794 EAAT2+ astrocytes based on laminar localisation (Layer II/III, Layer IV/V, Layer VI, and White Matter). Astrocyte density nominally increased in cases with profound stress during childhood (<12 years) compared to controls across all Layers (11-39%; VI-II; P=0.002-0.016), and 'no stress' cases, specifically in Layers (IV-

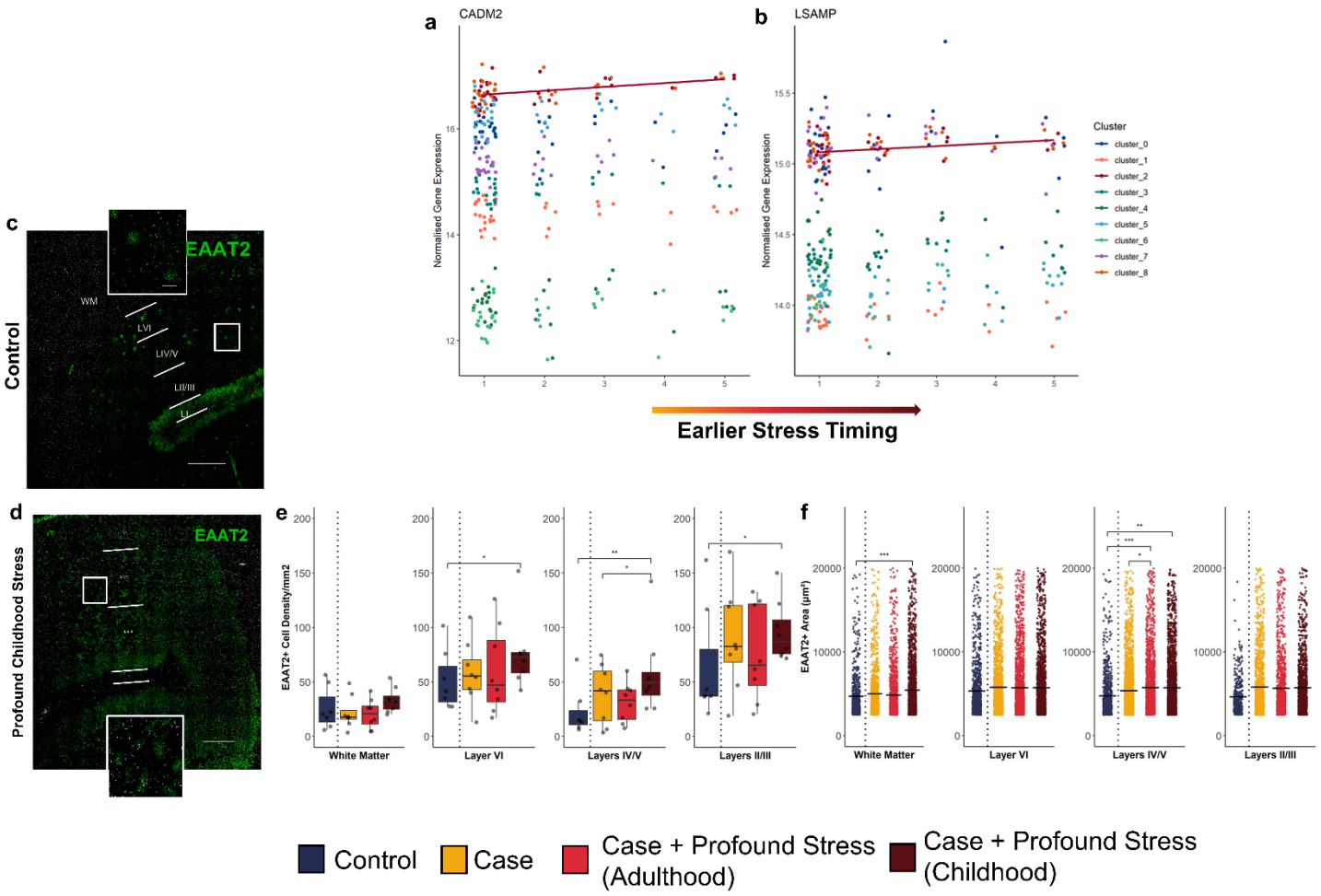

Figure 5: Earlier exposure to profound stress associates with greater alterations to astrocytes across transcriptomic and morphological measures. (a-b) Scatterplots for genes associated with stress timing. Normalised expression corrected for batch and covariates using limma removeBatchEffects (left to right: CADM2, LSAMP). Line indicates PFDR<0.05, colour indicates cluster. Stress timing - 5: childhood (<12), 4: adolescence [12-18], 3: early adulthood [18-25], 2: adulthood [25+] and 1: no profound stress prior to diagnosis). (d) Representative image of EAAT2 immunohistochemistry with representative automated segmentation used for morphology analysis. Scale bar = 1mm. (e) Density of EAAT2+ cells per mm2 by stress stratification and cortical layer. Box plots indicate median and quartiles. Significance calculated using linear regression on the log value correcting for covariates. *P<0.05,**P<0.01. (f) Area. Individual cell values are plotted. Line indicates mean. Significance calculated using linear regression on inverse value corrected for covariates as well as individual. P conservatively adjusted for number of cells using Bonferroni correction (n tests = number of cells). *Padj<0.05, **Padj<0.01, *Padj<0.001.

V) of the grey matter (20%; P=0.035), with only the childhood-control comparison in layers IV-V surviving testing for multiple comparisons (P_{adj}=0.014, Figure 5e). There was also an increase in the territory covered by EAAT2+ astrocytes across all profound stress cases in layers IV-V (adulthood: 21%, $P_{adj}=2.99\times10^{-5}$, childhood: 21%, $P_{adj}=2.43\times10^{-4}$) as well as an increase in the white matter (15%; $P_{adj}=2.31\times10^{-11}$) of those with childhood stress (Figure 5f). In further support that EAAT2+ astrocytes were distinctly impacted, we performed similar quantification with the total astrocyte marker SOX9[40] and found minimal changes to density with stress stratification in the grey matter (Supplementary Figure 9). This finding corroborates our transcriptomic evidence that there are detectable and persistent differences to astrocytes in human brains that have been exposed to pronounced stress. Importantly, these effects are not observed ubiquitously across cortical astrocyte populations nor spatial domains of the cortex, with astrocytes identified by expression of *SLC1A2* (EAAT2) in the grey matter disproportionately impacted.

Human astrocyte neurotransmission is sensitive to chronic glucocorticoid activation

Finally, we sought to explore how stress could directly shape astrocyte function in a human-relevant model. We applied GSEA to an existing transcriptomic dataset of cortisol-exposed human astrocytes derived from human induced pluripotent stem cells from female donors[41]. We identified 18 shared molecular functions with individuals diagnosed with a psychiatric disorder and prior history of stress (12 common to cluster 2, and 8 specifically with analysis in females), including G Protein-Coupled Receptor Binding and Glutamate Receptor Binding, modulators of glutamate signalling (Figure 6a).

To model whether functions related to glutamate signalling could be directly impacted by stress, we differentiated human astrocytes (iAsts) using lentiviral

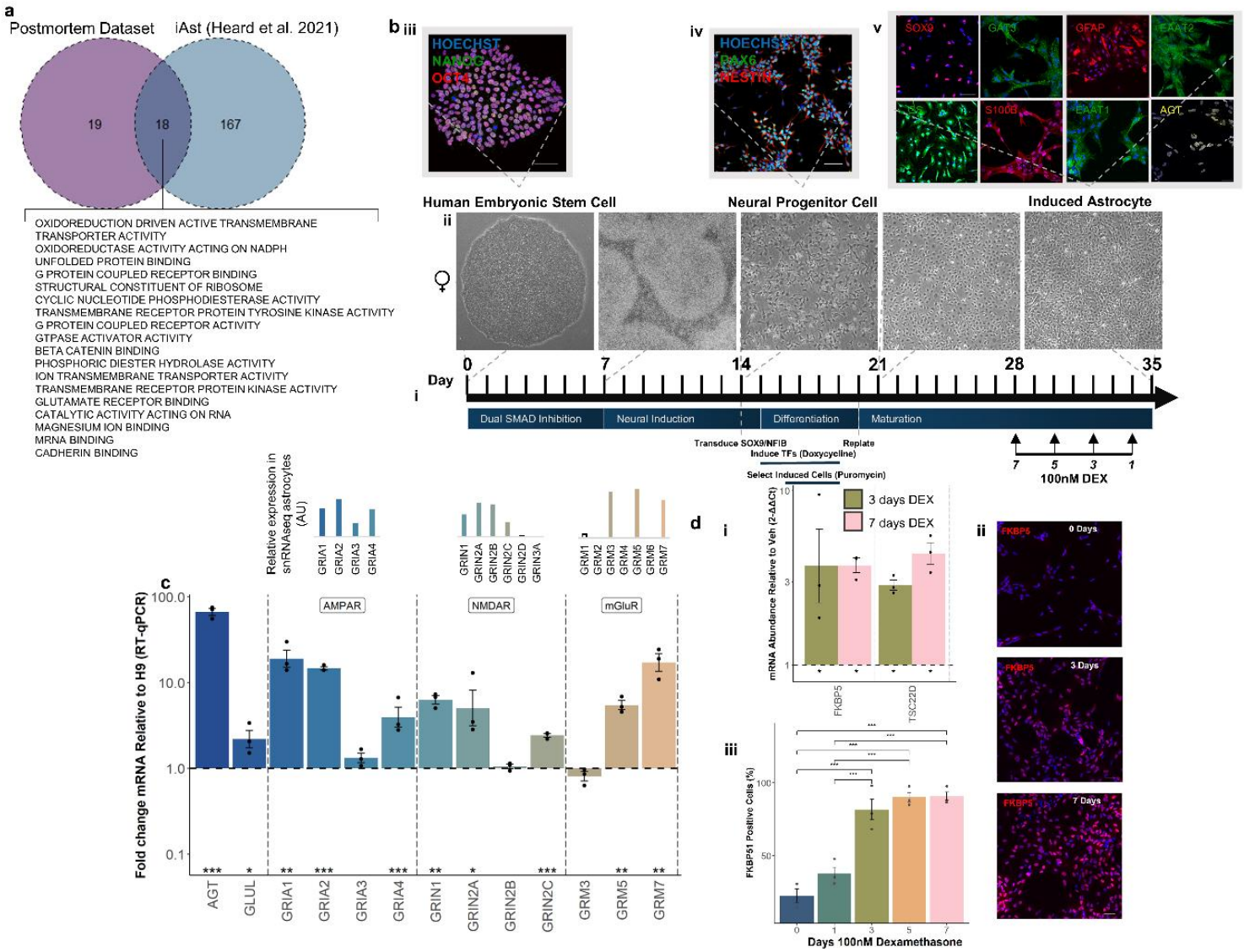

Figure 6: Human pluripotent stem cell-derived astrocytes can model specific dimensions of human astrocyte sensitivity to glucocorticoids. (a) Rank-rank hypergeometric overlap between bulk RNA seq of cortisol-exposed iAsts to human protoplasmic astrocytes from single nucleus RNA sequencing. B) Venn diagram of significant terms returned from all clusters and these iPSCS using the Molecular Function GO database. (b) Differentiation protocol used to derive astrocytes and expose them to dexamethasone: i) Timeline of differentiation; ii) Representative brightfield images of differentiation protocol; iii-v) Representative immunocytochemistry images from stages of differentiation validating expression of cell type markers. Scale bar = 50µm. (c) Fold change expression of genes in H9-derived iAsts compared to H9 stem cells. Astrocyte maturity markers (AGT and GLUL) and subunits of ionotropic (NMDA and AMPA) and metabotropic (GRM3/5/7) glutmate receptors. Bars represent mean value + 1SD. Graphs above represent relative expression of subunits in postmortem dataset in arbitrary units (AU) (d) Validation of response to glucocoritcoid paradigm: i) Fold change expression of glucocorticoid-responsive genes at 3 and 7 days of exposure relative to vehicle; ii) Representative immunocytocheemistry images with normalised FKBP5 staining at 0, 3, and 7 days of exposure; iii) Percentage of FKBP5 positive cells across timepoints. Calculated using ANOVA with post-hoc TukeyHSD. Bars represent mean value + 1SD. *P<0.05, **P<0.01, ***P<0.001. For all experiments, n=(3 biological replicates [different differentiations from hPSC] x 2 technical replicates [different well assayed]).

delivery of the transcription factors *SOX9* and *NFIB* to neural progenitors derived from the female hPSC line (H9) (Figure 6b i-iv)[42,43]. Synthesised iAsts expressed key astrocyte markers at both the RNA (qPCR; Figure 6c) and protein (immunocytochemistry; Figure 6b v) level, could effectively clear glutamate from media, and had robust calcium responses to agonists including glutamate and ATP (Figure 5; Supplementary Figure 10; Supplementary Figure 11). Importantly, the expression of glutamate receptor (NMDA and AMPA receptors) subunits largely resembled proportions observed in the snRNAseq dataset, except for the AMPA receptor subunit *GRIA3*, NMDA receptor subunit *GRIN2B*, and metabotropic glutamate receptor *GRM3* (Figure 6c). To mimic hormonal stress, iAsts were exposed to the glucocorticoid receptor agonist dexamethasone (100nM)[44]. The stress paradigm was conducted for durations of acute (12 hrs) to chronic (7 days), at which point the culture could not be effectively maintained due to increased proliferation (Supplementary Figure 12). This stress paradigm caused a dramatic increase in the expression of glucocorticoid-induced transcripts *TSC22D3* and *FKBP5* and cells immunopositive for FKBP51 by 3 days of treatment (Figure 6d).

First, we considered the role of astrocytes in clearing glutamate. While there was no significant effect on the

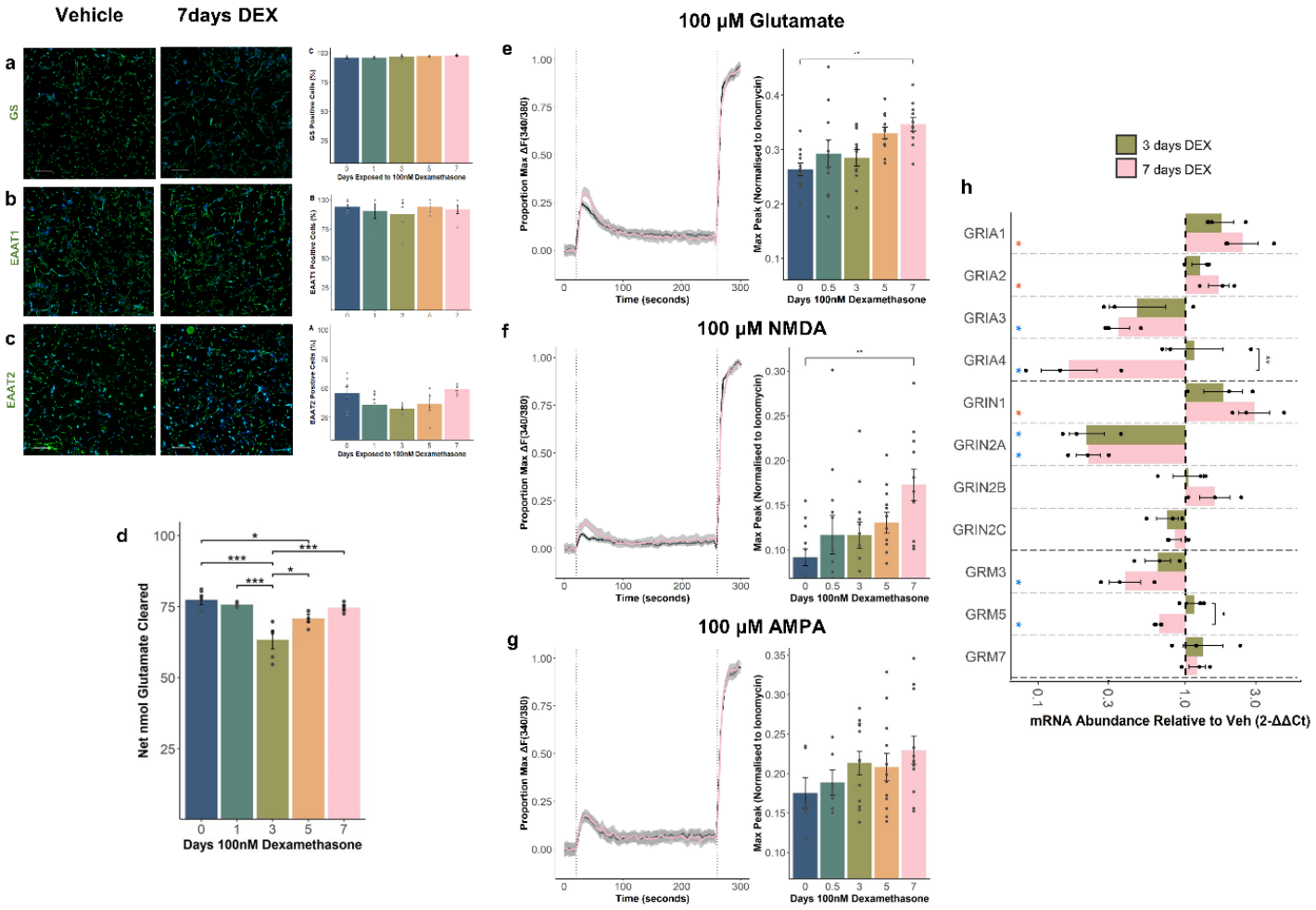

Figure 7: iAst glutamate homeostasis functions are directly shaped by glucocorticoid activation. (a-c) Representative images of iAsts with vehicle and after 7 days of dexamethasone exposure. Quantified number of positive cells at each timepoint (nuclei + protein/nuclei) (d) Glutmate clearance at each timepoint, normalised to total protein. (e-g) Whole-well ratiometric calcium signalling over time (proportion of 340/380nm wavelength emission). Data were normalised to maximum signal induced by ionomycin exposure. Traces indicate loess fit line on all replicates with span=0.05. Signifiance using was calculated using the maximum peak induced by agonist (between 0-200 seconds). (h) Fold change expression glutamate receptor genes at 3 and 7 days of exposure relative to vehicle. Blue asterisk indicates significantly reduced, and red increased. Signifiance calculated by ANOVA paired with TukeyHSD or linear regressions for pariwise comparisons. Bars represent mean value + 1SD. *P<0.05, **P<0.01, ***P<0.001. For all experiments, n= (3 biological replicates [different differentiations from hPSC] x 2 technical replicates [different well assayed])

number of EAAT1, EAAT2, or glutamine synthetase-positive astrocytes (Figure 7a-c), we did see a transient decrease in glutamate clearance after three days of stress, which was returned to untreated levels by seven days (Figure 7d). To expand upon this, we employed whole-well ratiometric Ca^{2+} imaging, to measure the maximal responses to glutamate, NMDA and AMPA agonism. After seven days of exposure, we observed that the maximum peak response of the iAsts to both glutamate and NMDA increased, relative to vehicle (8.3% increase, P=0.004; 8.1% increase, P=0.0047, respectively, Figure 7e-f). There were no significant differences in the Ca^{2+} response to AMPA following treatment with dexamethasone (Figure 7g).

To further dissect this, we quantified RNA expression of receptor subunits involved in coordinating direct Ca^{2+} responses, including NMDA, AMPA, and metabotropic receptors (mGluR3/5/7) (Figure 7h). We identified alterations to both NMDA and AMPA receptor subunits, with changes across all AMPA subunits (*GRIA1/GRIA2* up, *GRIA3/GRIA4* down), and NMDA subunits *GRIN1* (up) and *GRIN2A* (down). There were also modest decreases in the metabotropic receptors *GRM3/GRM5*, although the former was expressed at a low level. Notably, several of these effects were conserved with the study used to perform GSEA, including decreased *GRIA2/GRIA3/GRIA4* and *GRIN2A*.[41] Together, these studies demonstrate that astrocytes are directly sensitive to stress signalling, their functions in neurotransmission are actively shaped by stress, and that these functions can delineate cases of psychiatric disorders that have profound stress histories.

Discussion

This study profiled the transcriptome of >100,000 astrocytes and morphology of >20,000 astrocytes and considered these with spatial resolution. We detected transcriptional and morphological differences in astrocytes of individuals diagnosed with a psychiatric

disorder when stratified according to profound exposure to stress throughout life. We demonstrate that these effects are not equally shared across all astrocytes, nor spatial domains, between stress-stratified cases or between individuals with a psychiatric disorder diagnosis and controls. We also used hPSC-derived astrocytes to explore pathways directly altered by glucocorticoid signalling and demonstrate that astrocyte glutamate functions are directly sensitive to hormonal systems central to stress.

Prior snRNAseq approaches investigating psychiatric disorders have identified limited associations between astrocytes and either schizophrenia or major depression[10,13,45,46]. An important caveat with these approaches is that astrocytes are regularly conglomerated into a single population, while neuronal cell types are delineated into several classes, based on laminar and molecular phenotypes. While the cell type approach is crucial to narrowing broad and unbiased approaches, it likely masks heterogeneity existing in less defined cellular populations[47-49]. In our higher-resolution approach, we identified that both the transcriptomic and spatial diversity of astrocytes are relevant to psychopathology. This may be due to the greater number of astrocytes captured, which is 10-fold more than the average across several human studies[23]. Some evidence of variability has also been demonstrated in human psychopathologies. One study that performed qPCR on microdissected layers of the human anterior cingulate gyrus identified that several astrocyte markers, including the glutamate transporter EAAT2 and metabolising enzyme glutamine synthetase (GS), were selectively reduced in the deeper layers of the cortex (IV-VI), but not layers I-III nor in the white matter of individuals with schizophrenia[50]. Indeed, when we considered the astrocyte population at a bulk level (protoplasmic/fibrous), we observed no DEGs between the stress-stratified cases and only 10 DEGs between cases and controls. Our findings strengthen evidence of astrocyte diversity and its relevance to pathologies.

However, there is evidence of the transcriptional impact of stress on astrocytes from other species, even at a broad cell-type level. A recent snRNAseq and spatial analysis of the DLPFC from female macaque primates identified that astrocytes contributed the most DEGs associated with social stress[51]. In line with the present study, they identified that cell adhesion and glutamatergic synapse activity were over-represented terms associated with these DEGs, including decreased glutamine synthetase (*GLUL*), increased metabotropic (*GRM5*) and ionotropic (*GRIA1*, *GRIK2*) glutamate receptors in females. Female rodents have demonstrated divergent responses to cortical astrocytes, with only females demonstrating increased cell area in response to chronic restraint stress[52]. Estrogen can also increase EAAT2 expression and glutamate uptake in primary astrocyte culture[53]. Sex-specific temporal cues are important drivers of astrocyte maturation, with astrocytes in male rodents reaching maturity faster than in females[54], suggesting that the risk window for astrocyte sensitivity may diverge based on sex, and that sex hormones may influence this. Indeed, the hypothesis that stress occurring early in life when the brain is vulnerable is crucial to disorder onset has existed for decades[55-57] sex is likely a strong mediator of these changes[58]. Another study profiling the transcriptome of cortical astrocytes derived from male rodents exposed to chronic variable stress identified upregulation of *GRIA2* and *GRIA1*, in agreement with our glucocorticoid-treated iAsts[59]. The potential of these models to capture these changes at the bulk transcriptome level may also be partly due to their capacity to control the genetic and environmental conditions within the sample, something not possible in human studies.

The gene ontology terms emerging from this study indicate that the coordination (signalling and adhesion) of the synapse is a key system delineating profoundly stressed cases of psychiatric disorders. Reduced cortical synapses on excitatory neurons are one of the most well-documented phenomena associated with early life stress in rodents[11,60]. We have previously demonstrated that these effects are likely translationally robust. Using the same cohort used for morphological analysis we have identified reduced dendritic spines in cases with profound childhood stress[39], and that mature spine density is negatively correlated with stress modulators such as *FKBP5*[61]. A recent study demonstrated that cortisol activation of the glucocorticoid receptor directly mediated the pruning of excitatory synapses via astrocytes in both rodents and human-derived cortical organoids[62]. Importantly, this effect also attenuated behavioural symptoms associated with early social deprivation. Another study co-culturing mouse glia with human-derived neurons demonstrated that astrocytes coordinate the expression of several neuronal synaptic genes associated with schizophrenia[63]. They also noted that physical contact with astrocytes drove the expression of these genes, including *NRXN1*, a strong hit increased in association with stress in cluster 2. Recent snRNAseq evidence also suggests that astrocyte synapse functions are altered in schizophrenia and

further moderated by ageing[13]. This evidence supports that the modulation of synapses by astrocytes is a central system relevant to psychiatric disorders and that these systems are directly shaped by glucocorticoid signalling. Targeting astrocytes may, therefore be a promising target for novel therapeutics.

Finally, some key limitations of this study should be acknowledged. We used snRNAseq, not single cell RNA sequencing (scRNAseq), which expectedly limits the detection of genes related to ribosomes and mitochondria but also has relevance to glial cell states such as disease-associated microglia[64]. For most genes, however, it is largely concordant with single-cell approaches[65,66]. Another technical limitation was the inference of the snRNAseq onto the spatial transcriptomic domains. While we found parallel trends between imputed laminar distributions and immunohistology, more targeted methods may more faithfully capture transcriptomic changes associated with laminar populations (e.g. targeted laser capture paired with scRNAseq). Finally, the limited power in exploratory analyses (e.g. sex-specific and stress-timing analyses) necessitates replication.

Of note, iAsts most likely resemble late fetal astrocytes, and thus have limited transcriptomic similarity to mature human astrocytes (mean donor age in the present study > 50 years). The cellular environment around astrocytes is also likely not accurately represented by the 2D model[67-69]. This may limit th This study profiled the transcriptome of >100,000 astrocytes and morphology of >20,000 astrocytes and considered these with spatial resolution. We detected transcriptional and morphological differences in astrocytes of individuals diagnosed with a psychiatric disorder when stratified according to profound exposure to stress throughout life. We demonstrate that these effects are not equally shared across all astrocytes, nor spatial domains, between stress-stratified cases or between individuals with a psychiatric disorder diagnosis and controls. We also used hPSC-derived astrocytes to explore pathways directly altered by glucocorticoid signalling and demonstrate that astrocyte glutamate functions are directly sensitive to hormonal systems central to stress.

In summary, this study demonstrates that astrocytes are a highly diverse cell population and delineable across molecular, spatial, and morphological measurements when stratifying psychiatric disorder cases based on stress history. We identified that astrocytic coordination of the synaptic environment in the grey matter is a convergent system capable of delineating ‘stressed’ astrocytes from ‘unstressed’ astrocytes in humans, including in multi-transcriptomic, histological, and in vitro modalities. Our findings in astrocytes support that studies of psychiatric disorders at high resolution should aim to better reflect the clinical heterogeneity core to these disorders, for example stress exposure, as this will likely be essential to improving treatment specificity, and thus efficacy.

Methods

1.1 POSTMORTEM HUMAN BRAIN SAMPLES

Ethical approval for the study of postmortem human samples was obtained from the Human Ethics Committee at the University of Wollongong (HE 2020/308). The history of stressful events (childhood/adulthood) and psychiatric diagnoses (schizophrenia, schizoaffective disorder, depression, bipolar disorder) were extracted from extensive medical records of 92 adults (58 males, 34 females), as previously described[39,61]. Briefly, individuals were stratified based on whether they had a diagnosis of a severe psychiatric disorder, and whether they had been exposed to profound stress before disorder onset (32 no diagnosis, 32 with a diagnosis and with no profound stress, 28 with a diagnosis and with profound stress). Profound stress was considered an event, series of events, or set of circumstances that was physically or emotionally harmful or threatening and had lasting adverse effects on the individual's functioning and physical, social, or emotional well-being (e.g. physical/emotional abuse or neglect). From this cohort, fresh frozen tissue from the 3rd 8-10mm coronal section of Brodmann Area 11 (OFC) was used for all experiments. For single nucleus RNA sequencing, 87 samples produced high-quality libraries (one individual had low data quality and four had over 50% of nuclei were clustered in a single cluster) consisting of 32 controls, 31 cases with no pronounced stress, 24 cases with pronounced stress[76]. One sample was omitted from analysis related to psychopathology due to having a profound history of stress, but no noted psychiatric diagnosis. A subset of these histologically sound tissue structure cases were also processed for spatial transcriptomics (n=13). Finally, an overlapping subset (n=32, 27 individuals common between approaches), in which we have previously identified neuronal associations with childhood stress exposure[39], was used to explore the morphology of astrocytes. Groups had non-significant distributions of diagnoses, according to a chi-squared test (total: χ^2=1.83, P=0.61, snRNAseq:

χ^2=2.75, P=0.43). A schematic breakdown of the cohort, as well as key cohort demographics (diagnosis, age, sex, postmortem interval, RNA integrity, and brain pH) are detailed in Supplementary Figure 1.

1.2 SINGLE NUCLEUS RNA SEQUENCING

1.2.1 Sequencing, preprocessing, and broad cell type annotation

Nuclei were extracted and processed from fresh frozen postmortem brain tissue as described previously[76], with 10,000 nuclei per sample as target recovery. Briefly, samples were sequenced using the NovaSeq 6000 System and reads were aligned using Cell Ranger (Version 6.0.1) 'count' pipeline (genome build GRCh38, Ensembl 98). Reads per cell were downsampled to the 75% quantile and integrated in Python using Scanpy (Version 1.7.1)[77]. Preprocessing steps included filtering genes in <500 nuclei and cells with <500 counts, <300 genes, and/or >15% mitochondrial genes, doublet removal[42], and data normalisation and log-transformation using sctransform (Version 0.3.2)[78]. The Leiden clustering algorithm[79] based on highly variable genes was used to cluster nuclei (resolution 1.0). Cell types were assigned using a label transfer algorithm to infer primary cell types in clusters and high-resolution clusters were further manually annotated using marker genes as previously described[76]. Over 800,000 sequenced nuclei underwent quality control, clustering, and cell-type labelling[61,76]. a cluster of 113,140 nuclei labelled as astrocytes were isolated from this larger dataset for further analysis, using Scanpy for data processing (Version 1.9.6).

We then segregated and performed targeted re-clustering on these cells to explore heterogeneity at a higher resolution, identifying an initial 12 astrocyte clusters (Supplementary Figure 2). We removed two clusters given that one contained low-quality reads (high mitochondrial counts), and another was derived predominantly from two individuals.

1.2.2 Clustering astrocytes

In the astrocyte subset, highly variable genes and connectivity of neighbours were re-calculated. Dimensional reduction via uniform manifold approximation and projection (UMAP) was subsequently performed for visualisation. Appropriate clustering of astrocytes was determined using the Leiden algorithm. Stability analysis was conducted at resolutions 0.2-1.2 using two bootstrapping approaches. In the first, 90% of cells were subsampled and Leiden clustering with random seeding was applied across resolutions over 20 iterations. Stability per cluster was calculated as the mean value of all cells in that cluster being sorted into the same cluster. While the most stable clustering was at 0.2, 0.8 was selected due to its high local stability and capability to replicate clusters from prior studies (i.e. cluster 1) and to capture low cell count clusters (i.e. cluster 9; n=158 cells [0.14% of astrocytes]). To further support this, we used a second more stringent bootstrapping approach. Twenty iterations of Leiden clustering were applied to the whole dataset to determine baseline stability. A second round of 20 iterations was performed, removing the cells equivalent to one cluster at that resolution i.e. (1-1/n clusters). The difference in stability between these two iterative rounds was then determined. Marker genes per predicted cluster were determined using the rank_genes_groups function in Scanpy (method='Wilcoxon'), in accordance with recommendations with a recent benchmarking paper for marker gene selection.[80]

1.2.3 Differential expression analysis

Differential expression was conducted using limma (version 3.18, R)[81]. First, pseudobulk counts (the sum of raw counts per cluster, per individual) were calculated using ADPBulk (Python), and variance partitioning was performed on pseudobulk counts from all individuals using VariancePartition (R, version 1.28.9) fitting for measured covariates[82]. Variance partitioning identified strong effects of processing batch effects, high association of sex-specific genes (*UTY*, *XIST*) with sex, brain pH with ribosomal genes (*RPS27*, *RPL35*) and a significant proportion of variance unexplained by captured cohort demographics (Supplementary Figure 6). To correct for unexplained variance, the pseudobulk counts were first transformed using the limma voom transformation. The removeBatchEffect (limma) was then used to account for all full-rank covariates (Batch, Sex, Age, Postmortem Interval, RNA Integrity, Brain pH, Stress Stratification). Principal component analysis was then performed on the corrected counts and the resulting first principal component was included as a covariate in differential expression analysis to account for the high degree of unexplained variance. The final model used for differential expression was (~ library batch + sex + age + postmortem interval + RNA integrity + brain pH and PC1). All groups were included in the model, and pairwise comparisons between each of the groups was used to calculate DEGs. For sex-stratified analysis, the same approach was used, omitting the Sex variable from the model (~ library batch + age + postmortem interval + RNA integrity + brain pH and PC1). Extremely small pseudobulk

libraries <2000 reads were omitted. Analysis was conducted on robustly expressed genes with counts per million (CPM) >10 in at least 25% of the cohort, reflective of ~80% of the smallest group. DEGs were calculated between the stratified cases as well as healthy controls. Significance was considered any gene surviving a false discovery rate of 10% (P_{FDR}<0.1, Benjamini-Hochberg correction). We omitted cluster 9 from differential expression analysis due to low cell number.

1.2.4 Gene set enrichment analysis

Gene set enrichment analysis was performed on the entire transcriptome expressed at > 10 CPM using either cluster markers or DEGs using fGSEA (version 3.18, R). For cluster markers, rank was calculated as the gene score from the Wilcoxon test. For DEGs, rank was calculated as in a previous report[14] (nominal P * log2FoldChange) and gene ontology databases (Biological Processes, Molecular Function, Cellular Compartment) were accessed via msigdb (msigdbr version 7.5.1, R). For visualisation, terms were pruned based on semantic similarity, using GO.db (version 3.16.0, R) to access the GO directed graphs. Terms were only kept for visualisation if they had no nominally significant child terms (P<0.05). Full, unpruned lists are presented in Supplementary Data S3. Significance was set at P_{adj}<0.05.

1.2.5 Gene-disease association (DisGenNET)

The online tool EnrichR was used to access gene ontology databases, including DisGeNET[83]. Unranked DEG lists (P_{FDR}<0.1) were input and resulting gene ontology terms were sorted according to combined score. Significant terms were considered those with P_{adj}<0.05.

1.2.6 Rank-rank hypergeometric overlap

Threshold-free comparison between male and female DEGs was performed using rank-rank hypergeometric overlap (RRHO) analysis using the RRHO2[84]. Genes were scored using score = logFC *-$\log_{10}$P. Scored gene lists were initialised using the RRHO_initialise function (method = 'hyper', log10.ind=TRUE) and visualised using a heatmap. The colour of the heatmap was set to an upper limit of -logP=50 for consistency across graphs. The direction and strength of DEG correlation was further calculated using Spearman's correlation.

1.3 SPATIAL TRANSCRIPTOMICS

1.3.1 Library preparation (Visium)

Fresh frozen orbitofrontal cortex (BA11) sections (10µm thick) spanning all cortical layers were mounted onto capture areas on Visium (10x Genomics) spatial transcriptomics slides (6 x 6 mm) in a cryostat and then fixed in methanol for 30 mins at -20 ºC. Tissue was incubated sequentially in haematoxylin for 7 min, bluing buffer for 2 min, and eosin for 1 min. Histology of stained tissue sections were imaged using a Leica SP8 microscope (Wetzlar, Germany, objective: HC PL APO 10x/0.40 CS2). Following imaging, sections were permeabilised for 18 mins, according to prior optimisation, and libraries were prepared per the manufacturer's protocol. Libraries were pooled and sequencing was performed in a single run across 4 lanes on a NovaSeq v1.5 with an estimated library size of >115,000 read pairs per spot. In total, we detected 48,154 spots (2,645-4,422 per slide) with 109,893 (67,462-165,669) mean UMIs per spot and 90% of these mapped confidently to the genome (Supplementary Data S11).

1.3.2 Pre-processing

Read pairs were processed and aligned to a reference genome using Space Ranger (10x Genomics, Version 2.1.0) using the 'count' pipeline (genome build GRCh38, Ensembl 98). Aligned reads were preprocessed using Scanpy. Individual sections were normalised for library length (normalise_total), log transformed (log1p), and then concatenated into a unified dataset. The union of the 3000 most highly variable genes from each section were used to train the STAligner[85] tool on the points from all slides, with prior calculated spatial networks (Cal_Spatial_Net [rad=300]). Mitochondrial and haemoglobin genes were omitted from training the model due to their association with sample quality. On the concatenated dataset, spots containing <100 genes, <100 total counts and/or >85% mitochondrial genes were removed (all spots were retained until the spatial integration was completed to retain integrity of spatial graphs). Neighbours were calculated using the STAligner output and the mclust algorithm was then used to cluster the spatial domains (7 clusters, selected based on layers I-VI and white matter). Spatial domains were visually confirmed across all sections to validate that conserved laminar structure was retained across individuals. Cluster/layer markers were determined using rank_genes_group (Wilcoxon). We were unable to robustly delineate layer I from layer II due to the thinness of this domain in BA11 but

detected robust annotations for layers II-VI and white matter.

1.3.3 Single nucleus cell type spatial deconvolution

To map cell types from the whole snRNAseq dataset onto the spatial domains, the cluster mode of Tangram[31] was used to predict the probability of cell types at each point of the integrated spatial dataset, using the intersecting 10,000 most highly variable genes over 1000 epochs. A recent benchmarking study recommended Tangram for datasets where snRNAseq and spatial transcriptomics have been derived from the same individuals.[23] The calculated probability of each cell type at each spot was then multiplied by the total number of cells detected for that given cell type to obtain spatial and proportional distribution of cell types across the layers, relative to their abundance within the whole cell population.

To spatially resolve astrocyte subtypes, Tangram was used to impute the most probable layer onto each astrocyte nucleus. To prioritise astrocyte-relevant genes, genes with < 500 counts in < 1000 astrocyte nuclei were omitted before the clusters mode was trained on the intersecting 10,000 most highly variable genes from the spatial transcriptomics data over 1000 epochs, providing a probability of each cell occurring at each laminar domain. Each cell was then assigned to the most probable layer and cells with <1.5 fold change probability from other clusters were omitted for downstream analysis.

To explore the layer-specific astrocyte markers, a pseudobulked counts approach was performed reflective of the snRNAseq dataset. No covariates were included in this model, given that each individual was equally represented between layer measurements.

1.4 IMMUNOHISTOCHEMISTRY

Fresh frozen OFC sections (10µm thick) were mounted onto SuperFrost microscope slides and were then thawed for 10 mins at 37ºC and post-fixed in 4% paraformaldehyde for 15 mins at room temperature (RT). Sections were then blocked using 10% Normal Donkey Serum (Merck), 1%w/v Bovine Serum Albumin (Sigma), and 0.3M glycine (Sigma) in TBS for 1h at 37ºC. Sections were incubated in primary antibody diluted to the corresponding ratio in antibody diluent: (1% BSA, 0.3% Triton X-100 in TBS) overnight at 4ºC (Supplementary Table 1). The following day, secondaries (Donkey anti-rabbit Alexa Fluor Plus 488 [A32790], Donkey anti-rabbit Alexa Fluor Plus 647 [A32787]) and HOECSHT336 (ThermoFisher) were diluted in antibody diluent for 1h at RT, treated with 0.03%w/v Sudan Black in 70% ethanol for 20 mins and coverslipped using Fluromount (Sigma). Each step was washed 3 x 5 mins in TBS-Tween 20.

1.5 ANALYSIS OF ASTROCYTE MORPHOLOGY

Tissue sections were imaged on a Leica DMi8 fluorescent microscope (Leica DFC9000 GTC camera: 4.2 MP sCMOS camera) with an LED source, fitted with THUNDER image clearing. Whole tilescan images of cortical tissue were cleared using the Large Volume Computational Clearing. Astrocytes were detected using QuPath[86] (version 0.4.4), controlling for detection parameters across samples (fluorescence threshold=500, minimum/maximum area=1000/200000µm^2, sigma=6µm). Layer domains were identified using the morphological features of the nuclei and manually annotated. Cell density was measured as detected objects per annotation area. Area coverage of each identified cell was extracted per object and annotated per domain.

1.6 INDUCED ASTROCYTE DIFFERENTIATION FOR GLUCOCORTICOID ACTIVATION

1.6.1 Stem cell maintenance

All experiments using human pluripotent stem cells (hPSCs) were approved by the University of Wollongong Human Research Ethics Committee (HREC 2020/451) and the Institutional Biosafety Committee (Exempt Dealing GT19/08). H9 hPSCs (WA-09, WiCell) were cultured in mTeSR1 media (Stem Cell Technologies, Vancouver, Canada) in feeder-free conditions on Matrigel (Corning, New York, United States) coated plates. Media was changed daily. When cells reached 70-80% confluency, culture was dissociated with Accutase (Life Technologies) and ~10% of these cells were seeded as colonies. Thawed cells underwent two passages prior to the commencement of differentiation.

1.6.2 Lentiviral production

Lentivirus was produced using a 3rd generation lentivirus system. Plasmid DNA (pVSVG [addgene #8454], pRSV-Rev [#12253], pMDL/pRRE [#12251] and either FUW-M2rtTA [#20342] or the SOX9/NFIB plasmid[42] were complexed with PEI for 10 mins at 4˚C at a ratio of 1:2.5. HEK293T cells greater than 80%

confluency were transfected with plasmid complex for 2 h at 37˚C and lentiviral particles collected as in previous description.[87]

1.6.3 Astrocyte differentiation

To generate induced astrocytes (iAsts), we utilised a system that exploits the over expression of transcription factors key for astrocyte lineage determination, as described in prior papers[42,88,89]. First, neural progenitor cells (NPCs) were produced according to previously described protocols[90,91]. Briefly, colonies of hPSCs were maintained until colonies were at least 70% confluent. To induce neural fate, media was switched to a DMEM base containing 100nM LDN193189 and 10µM SB431542, supplemented with 1X B27 and 1X Glutamax. After seven days, the media was switched to a media containing 20ng/mL EGF and 20ng/mL FGF2 for an additional seven days. The resulting NPCs were dissociated using Accutase and cryobanked.

To generate iAsts, NPC stocks were plated onto Matrigel-coated places in the EGF/FGF2 media alongside 1µM Y-27632 and both TTA and SOX9-NFIB lentiviruses (Day 14). The virus was removed after 12-16 h and media was replaced with Astrocyte Differentiation Media (1% B27 supplement, 2mM GlutaMAX, 1% FBS, 8ng/mL FGF-2, 5ng/mL CNTF, 10ng/mL BMP4) containing 2µg/mL Doxycycline (Day 15). To select for transduced NPCs, media was further supplemented with 2µg/mL puromycin (Day 16-19). On day 20, induced iAst lineage cells were replated for downstream applications in Astrocyte Differentiation Media supplemented with Y-27632. After 8-12h, media was replaced with Maturation Media (1% N2, 1mM Sodium Pyruvate, 2mM GlutaMAX, N-acetyl-cysteine 5µg/mL, 5ng/mL heparin-binding EGF-like factor, 10ng/mL CNTF, 10ng/mL BMP4, 100µM DBcAMP). iAsts were cultured in Maturation Media for an additional 15 days (days 20-35).

1.7 Dexamethasone stimulation

To model the stress response in iAsts, glucocorticoid receptors were activated with 100nM equivalent dexamethasone (water-soluble) (Sigma-Aldrich, D2915) supplemented directly into Maturation Media. Cells were exposed for 0,0.5, 1, 3, 5, or 7 days prior to endpoint (day 35) with complete media replacement every 48 h. All treatments had the same endpoint for downstream assays.

1.8 Viability

Cell viability following dexamethasone treatment was determined using PrestoBlue (Invitrogen). Cells were incubated using a 1:10 dilution of reagent in Maturation Media for 30 mins at 37ºC. Viability was measured via fluorescence at excitation/emission of 560/590nm and normalised to wells containing only media.

1.9 Gene expression (qPCR)

RNA isolation was performed using a modified TRIsure (Bioline) method. iAsts were washed once with PBS and then incubated in 500µL TRIsure per well of a six-well plate for five mins at RT and manually agitated using a cell scraper. Chloroform was added in a 1:5 ratio to cell lysate, mixed for 15 s and incubated for a further 15 mins at RT. Samples were then centrifuged at 12,000g for 15 mins at 4°C. The aqueous phase was removed, mixed 1:1 with isopropanol, and frozen overnight at -80°C to precipitate the RNA. The samples were thawed on ice and centrifuged at 12,000g for 10 mins at 4°C to pellet RNA. Pellets were washed with 900 µL 75% ethanol, centrifuged, and left to air dry. Dried RNA was resuspended in 20-50µL RNase-free water and further treated with a Turbo DNA-free kit as per instructions to remove genomic DNA. RNA was then treated with 10% 4M Sodium Acetate and 1:10 isopropanol and precipitated overnight at -80°C. Thawed RNA was pelleted at >20,000g for 20 mins at 4˚C. Pellets were washed in 70% ethanol and centrifuged for a further two mins at >20,000g at 4°C. RNA was left to dry and resuspended in 20-50 µL RNase-free water. Yield and purity were determined using a NanoDrop 2000 spectrophotometer. One microgram of total RNA was reverse-transcribed to cDNA using the High-Capacity RNA-to-cDNA Kit (Thermo Fisher) and stored at -20˚C. Quantitative PCR (qPCR) was performed using KiCqStart SYBR Green Master Mix (Merck) SensiFAST No-ROX Kit (Bioline). Additional RT-qPCRs were performed using pre-designed TaqMan assays with TaqMan Universal PCR Master Mix. Amplification was visualized and analysed using a Quantstudio5 system (Thermofisher). Gene expression was compared to the geometric mean the Ct of B2M, GAPDH, and HPRT1. All samples were run in triplicate for each probe.

1.10 Immunocytochemistry

For all immunocytochemistry, cells were plated into optical glass bottom black-walled 96 well plates. At indicated timepoints, cells were washed three times with TBS and fixed with 4% PFA for 20 mins at RT,

followed by another three washes in TBS. Cells were permeabilised for 5 mins in 0.5% Triton X-100. Samples were blocked for 1h in TBS containing 5% normal donkey serum and 3% BSA, and then incubated in primary antibody solution (as above for IHC) at the indicated dilutions overnight at 4˚C (Supplementary Table 1). The following day, slides were washed three times with PBS and incubated in the respective secondary antibodies diluted 1:500 in antibody solution. Slides were washed three times and stored in a mounting medium consisting of 0.5% n-propyl gallate, 20nM Tris pH8.0, and 90% glycerol in water.

Cells were imaged using the same DMI8 setup as for the tissue but using small volume computational clearing. Positive cells were identified using QuPath, detecting the nuclei and expanding the radius 10µm and to capture the dual labelling in the cell body. Baseline settings were calibrated to control cells and maintained across all timepoints per protein visualised.

1.10.1 Glutamate uptake assay

iAsts were plated into Matrigel-coated 48 well plates. On Day 20, media was removed, washed one with Hanks Buffered Salt Solution (HBSS) (140mM NaCl, 5mM KCl, 1mM CaCl, 0.5mM MgCl, 0.3mM NaPO4, 0.4mM KHPO4, 6mM Glucose, 4mM NaHCO3) and equilibrated in fresh HBSS for 20 mins at 37ºC. Media was then replaced with HBSS supplemented with 150uM L-Glutamic Acid (Sigma). Media was collected off the cells at 120 mins post-exposure and stored at -20ºC. Controls consisting of Na+-free HBSS (NaCl replaced with equimolar Choline Chloride) and dl-threo-b-hydroxyaspartic acid, a potent inhibitor of EAAT family proteins, including EAAT1/2 were performed in parallel to validate efficacy of glutamate clearance. Cells were immediately lysed in ice cold Radioimmunoprecipitation Assay (RIPA) buffer and protein was quantified using a Bradford Assay (Bio-Rad), per manufacturer's instructions.

Glutamate remaining in media was determined using a Glutamate Assay Kit (abcam, ab83389) following the provided protocol. Glutamate was subtracted from the glutamate treatment well containing no cells and normalized to the total protein of each well to determine relative glutamate uptake.

1.10.2 Calcium imaging

Astrocytes seeded at 10,000 cells per well of a black-walled clear plastic bottom 96 well plate were washed and loaded with 4µM Fura-2, AM and 0.02% Pluronic Acid in HBSS for 45 mins at 37ºC. Cells were then washed for 10 mins in HBSS and placed in a starting volume of 80µL HBSS. Calcium activity was measured using a Flexstation 3. Respective compounds (20µL) [final conc] (ATP [30µM], glutamate [100µM], GABA [100µM], AMPA [100µM], NMDA [100µM]) were added at 20 seconds and ionomycin [3µM] was added after 4 mins followed by another 1 min of imaging. The $F_{340/380}$ nm excitation ratio was measured every 4s at 510nm. Data was normalised to the first three readings (prior to compound addition). Peak response was taken as the highest normalised ratio measurement between 20 and 160 seconds. Maximum response was taken as the highest $F_{340/380}$ ratio after the addition of ionomycin. To determine the proportion of the maximum response, normalised baseline was subtracted from all values and peak response was normalised to maximum response.

References

1 Santomauro, D. F. *et al.* Global prevalence and burden of depressive and anxiety disorders in 204 countries and territories in 2020 due to the COVID-19 pandemic. *The Lancet* **398**, 1700-1712 (2021).

2 Hillis, S., Mercy, J., Amobi, A. & Kress, H. Global prevalence of past-year violence against children: a systematic review and minimum estimates. *Pediatrics* **137** (2016).

3 Charlson, F. *et al.* New WHO prevalence estimates of mental disorders in conflict settings: a systematic review and meta-analysis. *The Lancet* **394**, 240-248 (2019). https://doi.org:10.1016/s0140-6736(19)30934-1

4 Grummitt, L., Baldwin, J. R., Lafoa'i, J., Keyes, K. M. & Barrett, E. L. Burden of Mental Disorders and Suicide Attributable to Childhood Maltreatment. *JAMA psychiatry* (2024).

5 Kaplan, M. J. & Klinetob, N. A. Childhood emotional trauma and chronic posttraumatic stress disorder in adult outpatients with treatment-resistant depression. *The Journal of nervous and mental disease* **188**, 596-601 (2000).

6 Thase, M. E. Treatment-resistant depression: prevalence, risk factors, and treatment strategies. *J Clin Psychiatry* **72**, e18 (2011). https://doi.org:10.4088/JCP.8133tx4c

7 Fried, E. I., Nesse, R. M., Guille, C. & Sen, S. The differential influence of life stress on individual symptoms of depression. *Acta psychiatrica Scandinavica* **131**, 465-471 (2015).

8 Millman, Z. B. *et al.* Perceived social stress and symptom severity among help-seeking adolescents with versus without clinical high-risk for psychosis. *Schizophrenia Research* **192**, 364-370 (2018).

https://doi.org:https://doi.org/10.1016/j.schres.2017.06.002

9 Nugent, K. L., Chiappelli, J., Rowland, L. M. & Hong, L. E. Cumulative stress pathophysiology in schizophrenia as indexed by allostatic load. *Psychoneuroendocrinology* **60**, 120-129 (2015). https://doi.org:10.1016/j.psyneuen.2015.06.009

10 Chatzinakos, C. *et al.* Single-Nucleus Transcriptome Profiling of Dorsolateral Prefrontal Cortex: Mechanistic Roles for Neuronal Gene Expression, Including the 17q21. 31 Locus, in PTSD Stress Response. *American Journal of Psychiatry* **180**, 739-754 (2023).

11 Kaul, D., Schwab, S. G., Mechawar, N. & Matosin, N. How stress physically re-shapes the brain: Impact on brain cell shapes, numbers and connections in psychiatric disorders. *Neuroscience & Biobehavioral Reviews* **124**, 193-215 (2021). https://doi.org:https://doi.org/10.1016/j.neubiorev.2021.01.025

12 Kenwood, M. M. *et al.* Gene expression in the primate orbitofrontal cortex related to anxious temperament. *Proceedings of the National Academy of Sciences* **120**, e2305775120 (2023).

13 Ling, E. *et al.* A concerted neuron–astrocyte program declines in ageing and schizophrenia. *Nature*, 1-8 (2024).

14 Maitra, M. *et al.* Cell type specific transcriptomic differences in depression show similar patterns between males and females but implicate distinct cell types and genes. *Nature Communications* **14**, 2912 (2023).

15 Sofroniew, M. V. & Vinters, H. V. Astrocytes: biology and pathology. *Acta neuropathologica* **119**, 7-35 (2010).

16 Murphy-Royal, C., Ching, S. & Papouin, T. A conceptual framework for astrocyte function. *Nat Neurosci* **26**, 1848-1856 (2023). https://doi.org:10.1038/s41593-023-01448-8

17 Escartin, C. *et al.* Reactive astrocyte nomenclature, definitions, and future directions. *Nature neuroscience* **24**, 312-325 (2021).

18 de Ceglia, R. *et al.* Specialized astrocytes mediate glutamatergic gliotransmission in the CNS. *Nature* **622**, 120-129 (2023).

19 Yao, Z. *et al.* A high-resolution transcriptomic and spatial atlas of cell types in the whole mouse brain. *Nature* **624**, 317-332 (2023).

20 Kringelbach, M. L. & Rolls, E. T. The functional neuroanatomy of the human orbitofrontal cortex: evidence from neuroimaging and neuropsychology. *Prog Neurobiol* **72**, 341-372 (2004).

21 Pizzagalli, D. A. & Roberts, A. C. Prefrontal cortex and depression. *Neuropsychopharmacology* **47**, 225-246 (2022). https://doi.org:10.1038/s41386-021-01101-7

22 Kanahara, N. *et al.* Orbitofrontal cortex abnormality and deficit schizophrenia. *Schizophr Res* **143**, 246-152 (2013). https://doi.org:10.1016/j.schres.2012.11.015

23 Qian, Z., Qin, J., Lai, Y., Zhang, C. & Zhang, X. Large-Scale Integration of Single-Cell RNA-Seq Data Reveals Astrocyte Diversity and Transcriptomic Modules across Six Central Nervous System Disorders. *Biomolecules* **13**, 692 (2023).

24 Hodge, R. D. *et al.* Conserved cell types with divergent features in human versus mouse cortex. *Nature* **573**, 61-68 (2019).

25 Falcone, C. *et al.* Redefining varicose projection astrocytes in primates. *Glia* **70**, 145-154 (2022).

26 Bayraktar, O. A. *et al.* Astrocyte layers in the mammalian cerebral cortex revealed by a single-cell in situ transcriptomic map. *Nat Neurosci* **23**, 500-509 (2020). https://doi.org:10.1038/s41593-020-0602-1

27 Lanjakornsiripan, D. *et al.* Layer-specific morphological and molecular differences in neocortical astrocytes and their dependence on neuronal layers. *Nat Commun* **9**, 1623 (2018). https://doi.org:10.1038/s41467-018-03940-3

28 Batiuk, M. Y. *et al.* Identification of region-specific astrocyte subtypes at single cell resolution. *Nat Commun* **11**, 1220 (2020). https://doi.org:10.1038/s41467-019-14198-8

29 Maynard, K. R. *et al.* Transcriptome-scale spatial gene expression in the human dorsolateral prefrontal cortex. *bioRxiv*, 969931 (2020). https://doi.org:10.1101/2020.02.28.969931

30 Chen, S. *et al.* Spatially resolved transcriptomics reveals genes associated with the vulnerability of middle temporal gyrus in Alzheimer's disease. *Acta Neuropathologica Communications* **10**, 1-24 (2022).

31 Biancalani, T. *et al.* Deep learning and alignment of spatially resolved single-cell transcriptomes with Tangram. *Nature methods* **18**, 1352-1362 (2021).

32 Huuki-Myers, L. *et al.* Integrated single cell and unsupervised spatial transcriptomic analysis defines molecular anatomy of the human dorsolateral prefrontal cortex. *BioRxiv* (2023).

33 Lowe, S. R. *et al.* RORA and posttraumatic stress trajectories: main effects and interactions with childhood physical abuse history. *Brain Behav* **5**, e00323 (2015).

34 Velásquez, E. *et al.* Synaptosomal Proteome of the Orbitofrontal Cortex from Schizophrenia

Patients Using Quantitative Label-Free and iTRAQ-Based Shotgun Proteomics. *J Proteome Res* **16**, 4481-4494 (2017). https://doi.org:10.1021/acs.jproteome.7b00422

35 Labonté, B. *et al.* Sex-specific transcriptional signatures in human depression. *Nature medicine* **23**, 1102-1111 (2017).

36 Carr, C. P., Martins, C. M. S., Stingel, A. M., Lemgruber, V. B. & Juruena, M. F. The role of early life stress in adult psychiatric disorders: a systematic review according to childhood trauma subtypes. *The Journal of nervous and mental disease* **201**, 1007-1020 (2013).

37 Kaul, D. *et al.* Severe childhood and adulthood stress associates with neocortical layer-specific reductions of mature spines in psychiatric disorders. *Neurobiol Stress* **13**, 100270 (2020). https://doi.org:https://doi.org/10.1016/j.ynstr.2020.100270

38 Sun, W. *et al.* SOX9 Is an Astrocyte-Specific Nuclear Marker in the Adult Brain Outside the Neurogenic Regions. *J Neurosci* **37**, 4493-4507 (2017). https://doi.org:10.1523/jneurosci.3199-16.2017

39 Heard, K. J. *et al.* Chronic cortisol differentially impacts stem cell-derived astrocytes from major depressive disorder patients. *Translational psychiatry* **11**, 608 (2021).

40 Ng, N. S. *et al.* Edaravone and mitochondrial transfer as potential therapeutics for vanishing white matter disease astrocyte dysfunction. *CNS Neurosci Ther* **29**, 2481-2497 (2023). https://doi.org:10.1111/cns.14190

41 Canals, I. *et al.* Rapid and efficient induction of functional astrocytes from human pluripotent stem cells. *Nature methods* **15**, 693-696 (2018).

42 Carter, B. S., Meng, F. & Thompson, R. C. Glucocorticoid treatment of astrocytes results in temporally dynamic transcriptome regulation and astrocyte-enriched mRNA changes in vitro. *Physiological genomics* **44**, 1188-1200 (2012). https://doi.org:10.1152/physiolgenomics.00097.2012

43 Ruzicka, W. B. *et al.* Single-cell multi-cohort dissection of the schizophrenia transcriptome. *medRxiv*, 2022.2008.2031.22279406 (2022). https://doi.org:10.1101/2022.08.31.22279406

44 Nagy, C. *et al.* Single-nucleus transcriptomics of the prefrontal cortex in major depressive disorder implicates oligodendrocyte precursor cells and excitatory neurons. *Nat Neurosci* **23**, 771-781 (2020). https://doi.org:10.1038/s41593-020-0621-y

45 Escartin, C. *et al.* Reactive astrocyte nomenclature, definitions, and future directions. *Nat Neurosci* (2021). https://doi.org:10.1038/s41593-020-00783-4

46 Lozzi, B., Huang, T. W., Sardar, D., Huang, A. Y. & Deneen, B. Regionally Distinct Astrocytes Display Unique Transcription Factor Profiles in the Adult Brain. *Front Neurosci* **14**, 61 (2020). https://doi.org:10.3389/fnins.2020.00061

47 Verkhratsky, A., Zorec, R. & Parpura, V. Stratification of astrocytes in healthy and diseased brain. *Brain Pathol* **27**, 629-644 (2017). https://doi.org:10.1111/bpa.12537

48 Katsel, P. *et al.* Astrocyte and glutamate markers in the superficial, deep, and white matter layers of the anterior cingulate gyrus in schizophrenia. *Neuropsychopharmacology* **36**, 1171-1177 (2011).

49 Wu, J. *et al.* Integrating spatial and single-nucleus transcriptomic data elucidates microglial-specific responses in female cynomolgus macaques with depressive-like behaviors. *Nature Neuroscience* **26**, 1352-1364 (2023).

50 Bollinger, J. L., Salinas, I., Fender, E., Sengelaub, D. R. & Wellman, C. L. Gonadal hormones differentially regulate sex-specific stress effects on glia in the medial prefrontal cortex. *J Neuroendocrinol* **31**, e12762 (2019). https://doi.org:10.1111/jne.12762

51 Al-Bader, M. D., Malatiali, S. A. & Redzic, Z. B. Expression of estrogen receptor α and β in rat astrocytes in primary culture: effects of hypoxia and glucose deprivation. *Physiol Res* **60**, 951-960 (2011). https://doi.org:10.33549/physiolres.932167

52 Rurak, G. M. *et al.* Sex differences in developmental patterns of neocortical astroglia: A mouse translatome database. *Cell Reports* **38** (2022).

53 Meaney, M. *et al.* Sharma, JR Seckl, PM Plotsky, Early environmental regulation of forebrain glucocorticoid receptor gene expression: implications for adrenocortical responses to stress. *Dev. Neurosci* **18**, 49-72 (1996).

54 Sanacora, G., Yan, Z. & Popoli, M. The stressed synapse 2.0: pathophysiological mechanisms in stress-related neuropsychiatric disorders. *Nature Reviews Neuroscience* (2021). https://doi.org:10.1038/s41583-021-00540-x

55 McEwen, B. S. Understanding the potency of stressful early life experiences on brain and body function. *Metabolism* **57 Suppl 2**, S11-15 (2008). https://doi.org:10.1016/j.metabol.2008.07.006

56 Parel, S. T. & Peña, C. J. Genome-wide Signatures of Early-Life Stress: Influence of Sex. *Biol Psychiatry* **91**, 36-42 (2022). https://doi.org:10.1016/j.biopsych.2020.12.010

57 Simard, S. *et al.* Profiling changes in cortical astroglial cells following chronic stress. *Neuropsychopharmacology* **43**, 1961-1971 (2018). https://doi.org:10.1038/s41386-018-0105-x
58 Radley, J. J. *et al.* Repeated stress induces dendritic spine loss in the rat medial prefrontal cortex. *Cereb Cortex* **16**, 313-320 (2005). https://doi.org:10.1093/cercor/bhi104
59 Matosin, N. *et al.* Associations of psychiatric disease and ageing with FKBP5 expression converge on superficial layer neurons of the neocortex. *Acta neuropathologica* **145**, 439-459 (2023).
60 Byun, Y. G. *et al.* Stress induces behavioral abnormalities by increasing expression of phagocytic receptor MERTK in astrocytes to promote synapse phagocytosis. *Immunity* **56**, 2105-2120. e2113 (2023).
61 Pietiläinen, O. *et al.* Astrocytic cell adhesion genes linked to schizophrenia correlate with synaptic programs in neurons. *Cell Reports* **42** (2023).
62 Thrupp, N. *et al.* Single-nucleus RNA-Seq is not suitable for detection of microglial activation genes in humans. *Cell reports* **32** (2020).
63 Lake, B. B. *et al.* A comparative strategy for single-nucleus and single-cell transcriptomes confirms accuracy in predicted cell-type expression from nuclear RNA. *Scientific reports* **7**, 6031 (2017).
64 Ding, J. *et al.* Systematic comparison of single-cell and single-nucleus RNA-sequencing methods. *Nature biotechnology* **38**, 737-746 (2020).
65 Hasel, P. *et al.* Neurons and neuronal activity control gene expression in astrocytes to regulate their development and metabolism. *Nat Commun* **8**, 15132 (2017). https://doi.org:10.1038/ncomms15132
66 McGann, J. C. & Mandel, G. Neuronal activity induces glutathione metabolism gene expression in astrocytes. *Glia* **66**, 2024-2039 (2018). https://doi.org:10.1002/glia.23455
67 Sardar, D. *et al.* Mapping Astrocyte Transcriptional Signatures in Response to Neuroactive Compounds. *International Journal of Molecular Sciences* **22**, 3975 (2021). https://doi.org:10.3390/ijms22083975
68 Breen, M. S. *et al.* Global landscape and genetic regulation of RNA editing in cortical samples from individuals with schizophrenia. *Nature neuroscience* **22**, 1402-1412 (2019).
69 Choudhury, M. *et al.* Widespread RNA hypoediting in schizophrenia and its relevance to mitochondrial function. *Science Advances* **9**, eade9997 (2023).
70 Penner-Goeke, S. *et al.* High-throughput screening of glucocorticoid-induced enhancer activity reveals mechanisms of stress-related psychiatric disorders. *Proceedings of the National Academy of Sciences* **120**, e2305773120 (2023).
71 Liddelow, S. A. & Barres, B. A. Reactive astrocytes: production, function, and therapeutic potential. *Immunity* **46**, 957-967 (2017).
72 Liddelow, S. A. *et al.* Neurotoxic reactive astrocytes are induced by activated microglia. *Nature* **541**, 481-487 (2017).
73 Tynan, R. J. *et al.* Chronic stress-induced disruption of the astrocyte network is driven by structural atrophy and not loss of astrocytes. *Acta Neuropathologica* **126**, 75-91 (2013). https://doi.org:10.1007/s00401-013-1102-0
74 Wolf, F. A., Angerer, P. & Theis, F. J. SCANPY: large-scale single-cell gene expression data analysis. *Genome biology* **19**, 1-5 (2018).
75 Hafemeister, C. & Satija, R. Normalization and variance stabilization of single-cell RNA-seq data using regularized negative binomial regression. *Genome biology* **20**, 296 (2019).
76 Traag, V. A., Waltman, L. & Van Eck, N. J. From Louvain to Leiden: guaranteeing well-connected communities. *Scientific reports* **9**, 5233 (2019).
77 Pullin, J. M. & McCarthy, D. J. A comparison of marker gene selection methods for single-cell RNA sequencing data. *Genome Biology* **25**, 56 (2024).
78 Ritchie, M. E. *et al.* limma powers differential expression analyses for RNA-sequencing and microarray studies. *Nucleic acids research* **43**, e47-e47 (2015).
79 Hoffman, G. E. & Schadt, E. E. variancePartition: interpreting drivers of variation in complex gene expression studies. *BMC bioinformatics* **17**, 1-13 (2016).
80 Cahill, K. M., Huo, Z., Tseng, G. C., Logan, R. W. & Seney, M. L. Improved identification of concordant and discordant gene expression signatures using an updated rank-rank hypergeometric overlap approach. *Scientific reports* **8**, 9588 (2018).
81 Zhou, X., Dong, K. & Zhang, S. Integrating spatial transcriptomics data across different conditions, technologies and developmental stages. *Nature Computational Science*, 1-13 (2023).
82 Bankhead, P. *et al.* QuPath: Open source software for digital pathology image analysis. *Scientific reports* **7**, 1-7 (2017).
83 Newbery, M. *et al.* Efficient third generation lentiviral particle production. (2023).
84 Canals, I. *et al.* Rapid and efficient induction of functional astrocytes from human pluripotent stem cells. *Nat Methods* **15**, 693-

696 (2018). https://doi.org:10.1038/s41592-018-0103-2

85 Maksour, S. *et al.* REST and RCOR genes display distinct expression profiles in neurons and astrocytes using 2D and 3D human pluripotent stem cell models. *bioRxiv* (2024).

86 Denham, M. & Dottori, M. Neural differentiation of induced pluripotent stem cells. *Neurodegeneration: Methods and Protocols*, 99-110 (2011).

87 Ng, N. S. *et al.* An Optimized Direct Lysis Gene Expression Microplate Assay and Applications for Disease, Differentiation, and Pharmacological Cell-Based Studies. *Biosensors (Basel)* **12** (2022). https://doi.org:10.3390/bios12060364

a

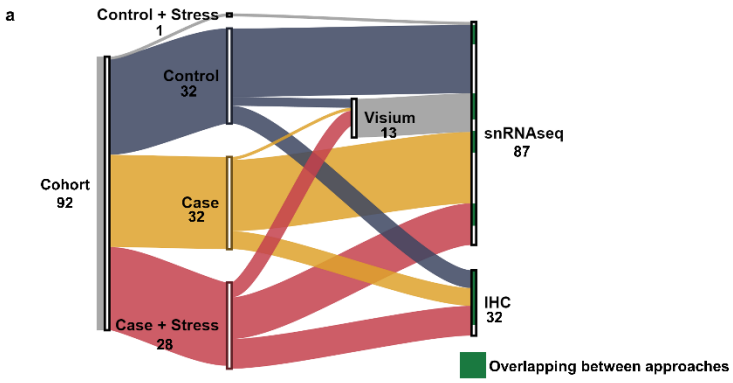

b

Total *N* (snRNAseq/ IHC/ Visium)	Classification	Profound Psychological Stress	Diagnosis (SCZ/MDD/ BPD/SZA)	Age (years) (Mean±SD)	Sex (M/F)	PMI (h) (Mean±SD)	RIN (Mean±SD)	pH (Mean±SD)
32	Healthy Control	No	-	**54.6±14.0**	**20/12**	**32.0±11.4**	**7.2±1.3**	**6.7±0.2**
31				57.3±12.7	20/11	30.6±11.0	7.2±1.4	6.7±0.2
8				49.0±17.9	5/3	34.4±4.4	7.9±0.2	6.7±0.1
3				55.1±15.7	3/0	32.2±10.2	8.0±0.6	6.8±0.1
1		Yes	-	-	-	-	-	-
32	Psychiatric Disorder	No	24/3/2/5	**52.4±11.6**	**19/13**	**32.3±13.4**	**7.3±1.5**	**6.6±0.2**
32				52.8±11.2	19/12	31.8±13.7	7.4±1.6	6.6±0.2
8				60.0±0.0	5/3	30.5±4.2	7.0±0.4	6.5±0.1
2				50.8±11.1	1/1	31.6±9.7	7.4±0.8	6.5±0.1
27		Yes	17/5/3/3	**52.5±16.4**	**19/8**	**37.3±19.0**	**7.2±1.5**	**6.6±0.3**
24				54.3±16.7	16/8	38.3±19.7	7.4±1.3	6.6±0.2
16				51.4±17.0	12/4	45.8±23.5	7.4±1.3	6.6±0.1
7				53.8±16.9	7/0	37.8±18.9	6.8±1.7	6.5±0.3

Supplementary Figure 1: Demographics of cohort used in study. (a) Alluvial plot illustrating breakdown of composition used for experiments. Green in final bar indicates proportion of individuals common to transcriptomic approaches and immunohistochemistry**. (b)** Table outlining key clinical covariates accounted for in this study. Abbreviations: SCZ: schizophrenia, MDD: major depressive disorder, BPD: bipolar disorder, SCA: schizoaffective disorder, M: Male, F: Female, PMI: postmortem interval, RIN: RNA integrity number.

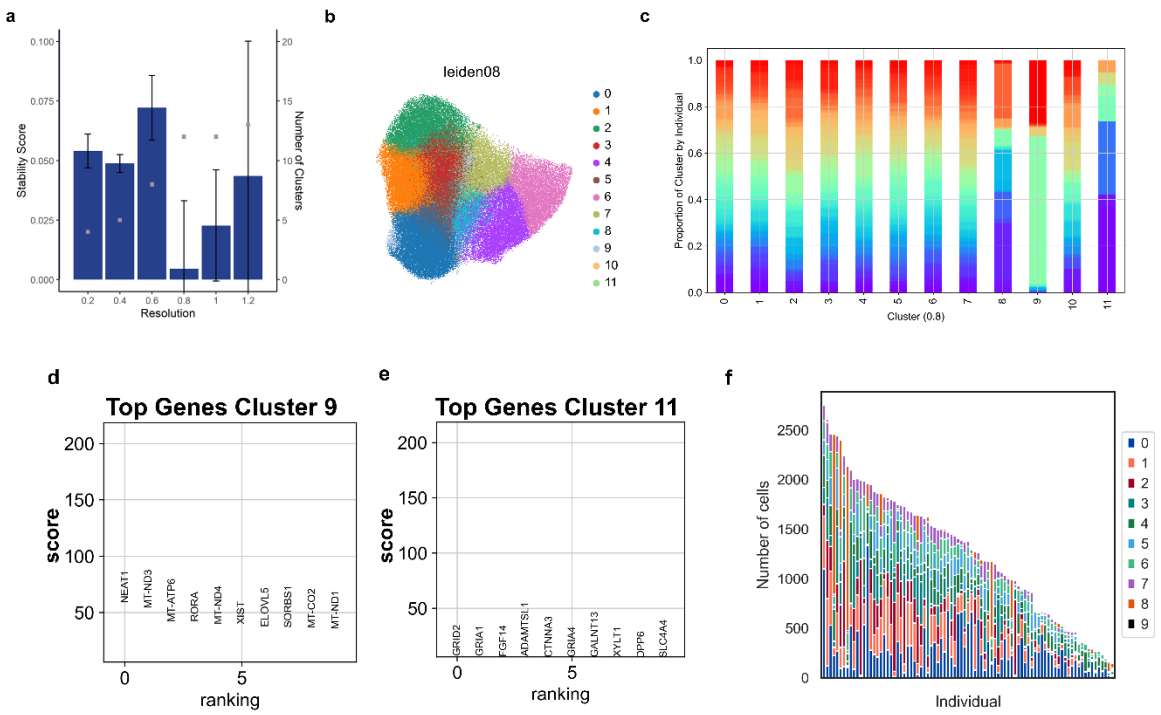

Supplementary Figure 2: Extended profiling of snRNAseq astrocyte clustering. (a) Cluster stability analysis using Leiden clustering at 0.2 increments. Deviation values between 20 iterations using the whole dataset and bootstrapping method run over 20 iterations using randomly selected n cells, where n cells are the proportion needed to remove a whole cluster (1 – 1/n clusters). Low value indicates better stability. Bars represent mean cluster stability (± 1SD). Grey points indicate number of clusters identified at each resolution. **(b)** Representative UMAP of initial clustering at selected resolution **(c)** Number of astrocytes per individual coloured by cluster number. **(d-e)** Top marker genes of removed clusters. **(f)** Cluster distribution per individual for tidied clusters.

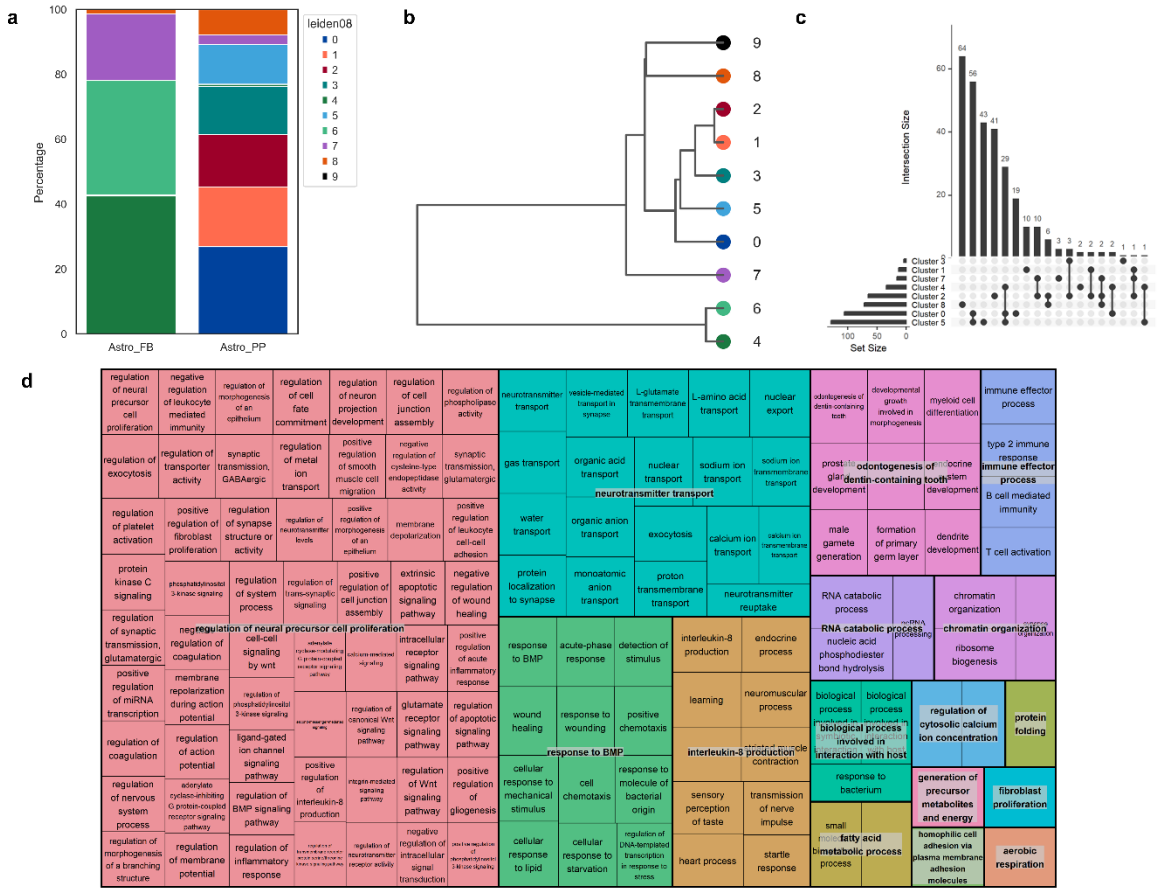

Supplementary Figure 3: Extended profiling of astrocyte cluster identity. (a) Proportion of astrocytes belonging to established identities. Broad cell types (Astro_FB/Astro_PP) were identified using label transferring approach on the whole cell population. Percentage of cells in each cluster belonging to broad identities as a percentage of all broad astrocyte cells plotted. **(b)** Dendrogram of cluster similarity based on the first 50 principal components. Pearson's correlation. **(f)** UpSet plot of intersection of C5 GO terms arising from gene set enrichment analysis. Set size indicates terms where P_{adj} <0.05. Overlapping terms indicated as levels connected by a line and intersection size indicates terms associated with this intersection. **(d)** Semantic similarity of snRNAseq significant GSEA terms. ReviGO was used to cluster significant C5 gene ontology terms using the SimRel similarity measure. Terms with grey background denote family terms associated with terms sharing colour/thick border.

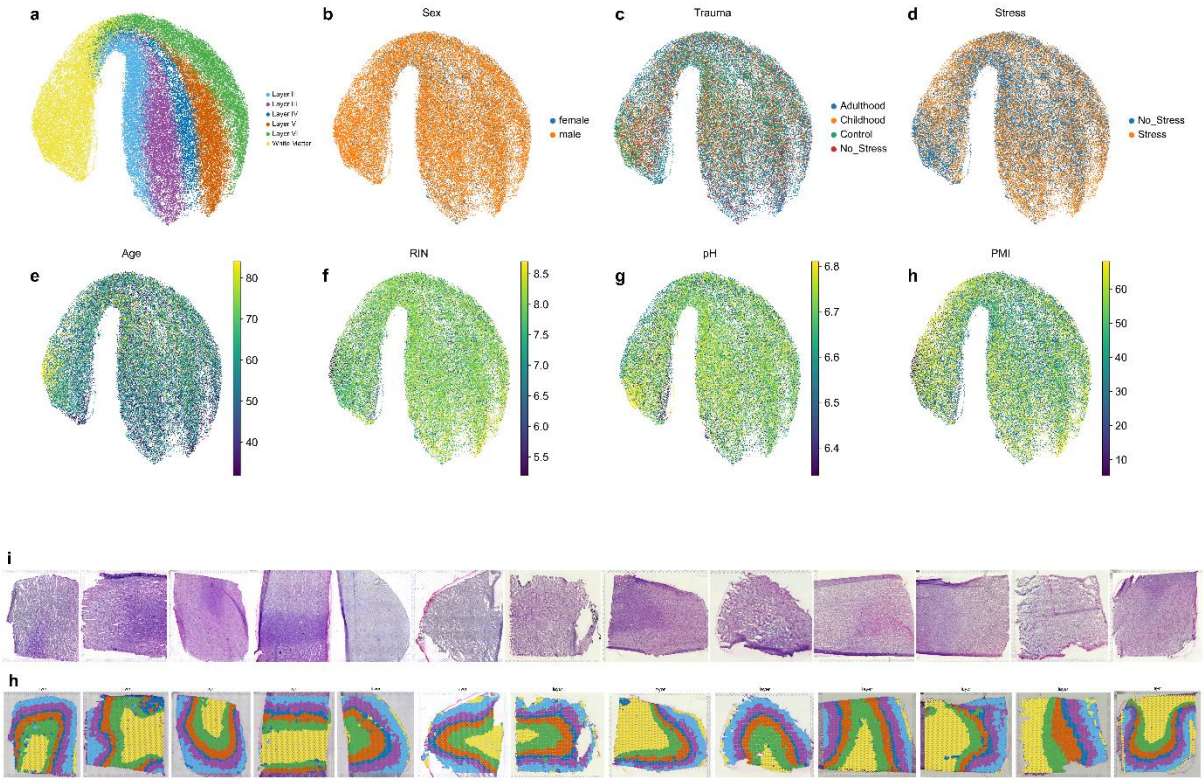

Supplementary Figure 4: Spatial transcriptomics clustering validation. (a-h) UMAP plot coloured by demographic covariates.**(i-h)** Histological validation of unbiased layer annotation. i) H+E staining of the capture regions containing the cortical sections used for spatial transcriptomics, demonstrating physical tissue quality across the cohort. h) remapping the unbiased integration of layer annotations back on to all sections used within the cohort demonstrates consistent laminar identification across the orbitofrontal cortex.

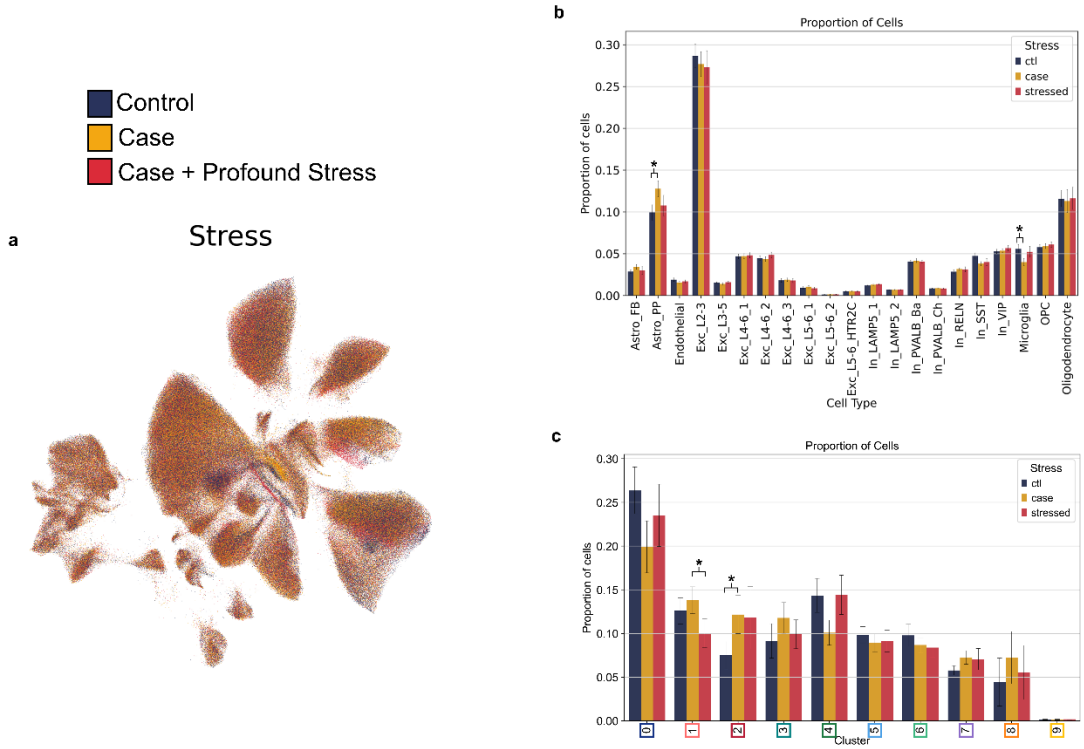

Supplementary Figure 5: Single nucleus RNAseq cell type proportions delineated by stress stratification. (a) 2D UMAP representation of snRNAseq dataset coloured by stress stratification. No cell type demonstrates biased clustering from any group. **(b)** Proportion of broad cell types grouped by stress stratification. Significance calculated using a linear regression correcting for sequencing batch. **(c)** Proportion of astrocyte subclusters grouped by stress stratification. Coloured border indicates cluster. Significance calculated using a linear regression correcting for sequencing batch. *P_{nom}<0.05.

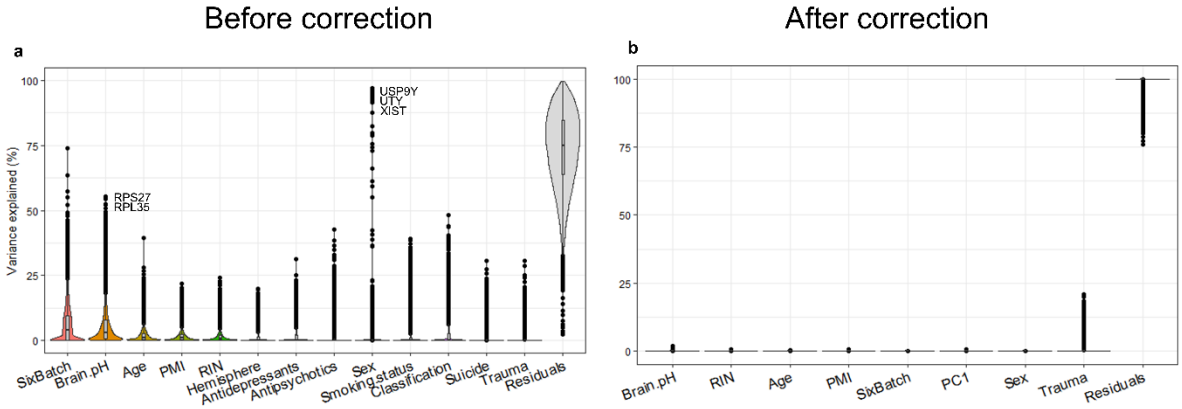

Supplementary Figure 6: Variance partitioning of single nucleus RNAseq. (a) Variance partitioning using pseudobulk counts for all astrocytes before batch correction. Representative genes demonstrate faithful partitioning of covariate-associated genes. **(b)** Variance partitioning using pseudobulk counts for all astrocytes after batch correction demonstrates that the method reduces both covariate noise as well as unexplained residuals, corrected for with PC1.

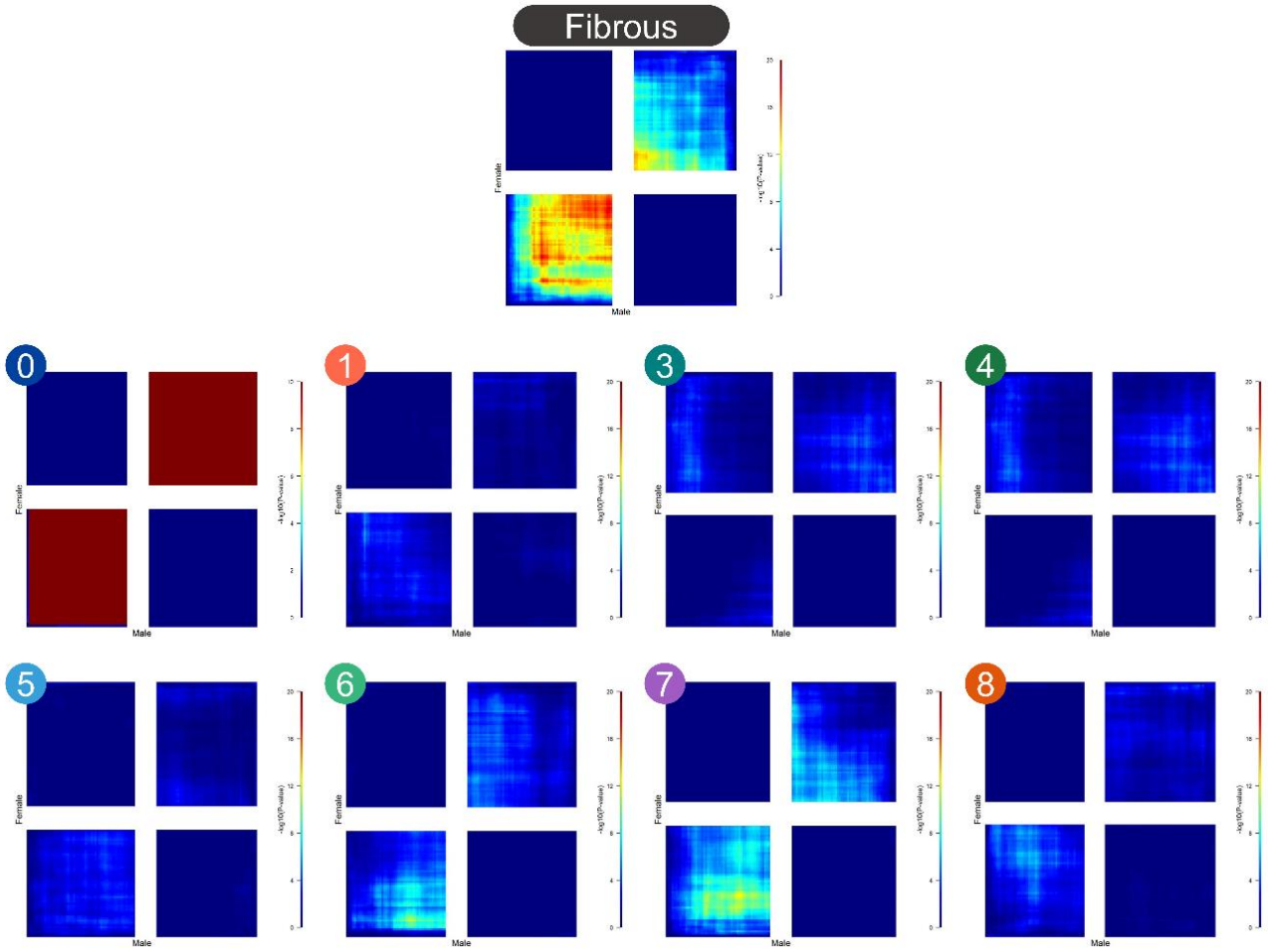

Supplementary Figure 7: Rank rank hypergeometric overlap between male and female DEGs (profound stress cases vs no profound stress cases) by cluster. Scale set to -log10P 0-20.

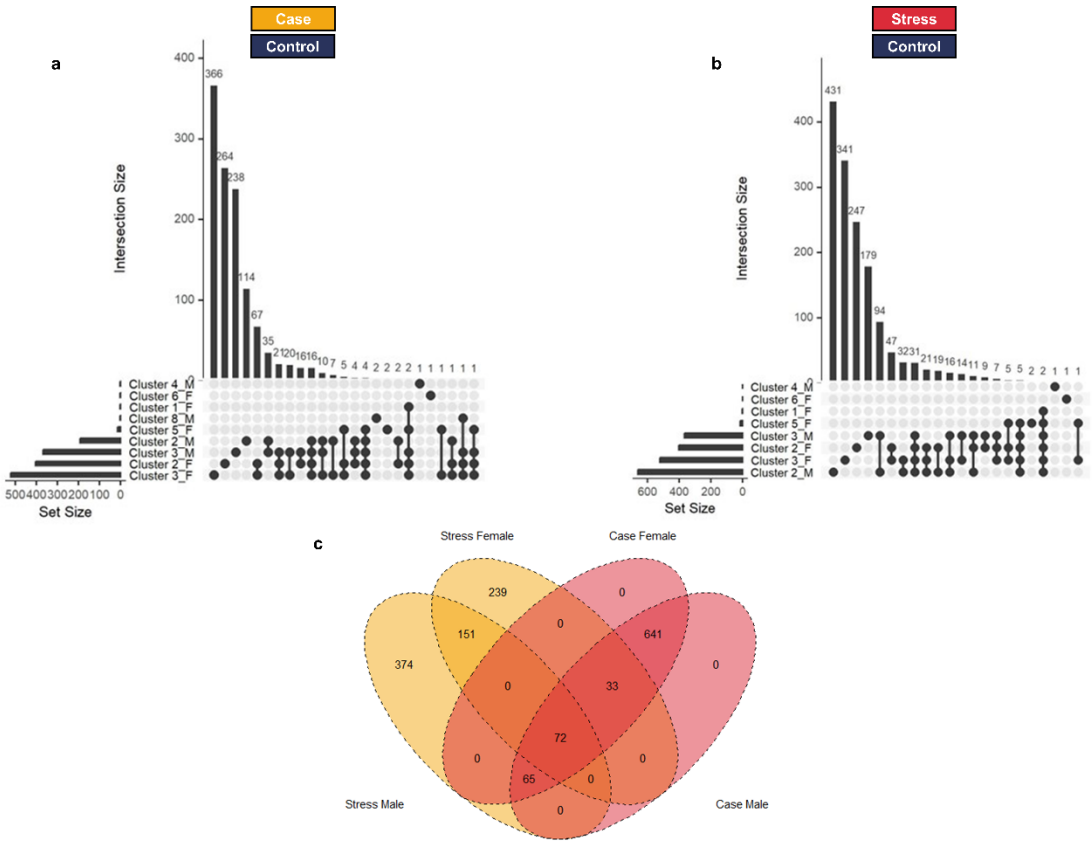

Supplementary Figure 8: Differentially expressed genes between cases and controls by sex. (a) UpSet plot of DEGs between cases with no profound stress and controls by sex (P_{FDR}<0.1). Set size indicates number of genes meeting threshold for each cluster and dots connected by a line indicate common genes. **(b)** UpSet plot of DEGs between cases with profound stress and controls by sex (P_{FDR}<0.1). Set size indicates number of genes meeting threshold for each cluster and dots connected by a line indicate common genes. **(c)** Venn diagram of total DEG overlap by profound stress (stress) or not (case).

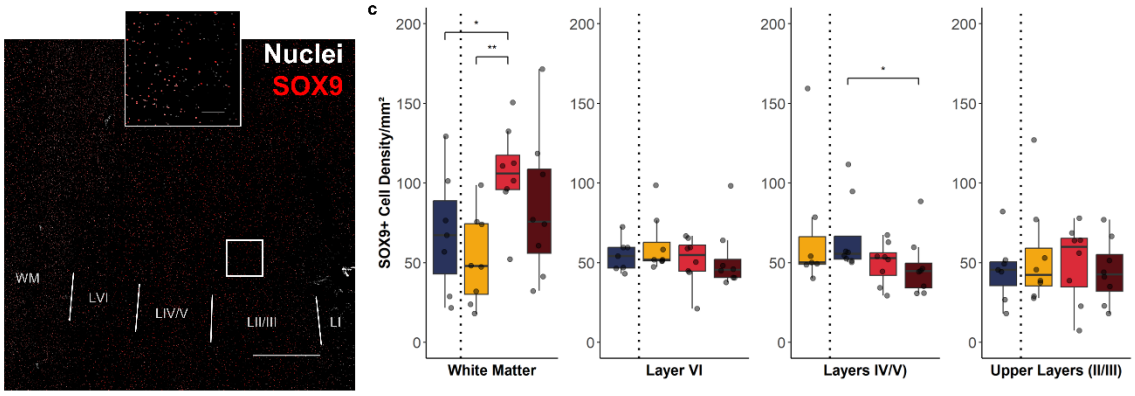

Supplementary Figure 9: Quantification of SOX9 immunohistochemistry. (a) Representative whole coronal section used for quantification of SOX9. **(b)** Selected region demonstrating close-up staining. Scale bar on tilescan indicates 1mm, and 100µm in magnified region. **(c)** Quantification of the density of SOX9+ cells per mm^2 by layer by stress timing stratification. Significance: *P<0.05, **P<0.01

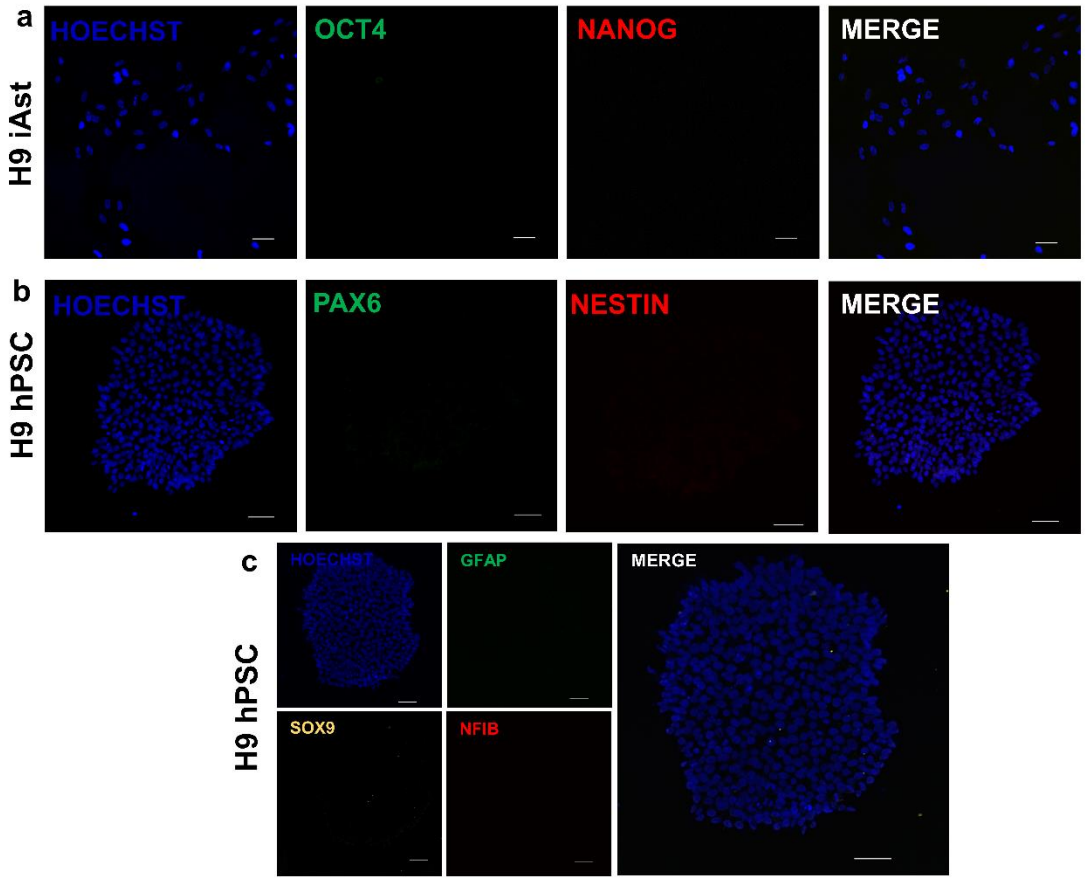

Supplementary Figure 10: Immunocytochemical negative controls for cell types. (a) Validation that iAst do not express pluripotency markers, OCT4 (green) and NANOG (red). **(b)** Validation that H9 human pluripotent stem cells do not express neural progenitor markers, PAX6 (green) and NESTIN (red). **(c)** Validation that H9 human pluripotent stem cells do not express astrocyte markers GFAP (green), SOX9 (yellow) and NIFB (red). Scale bar indicates 50µm.

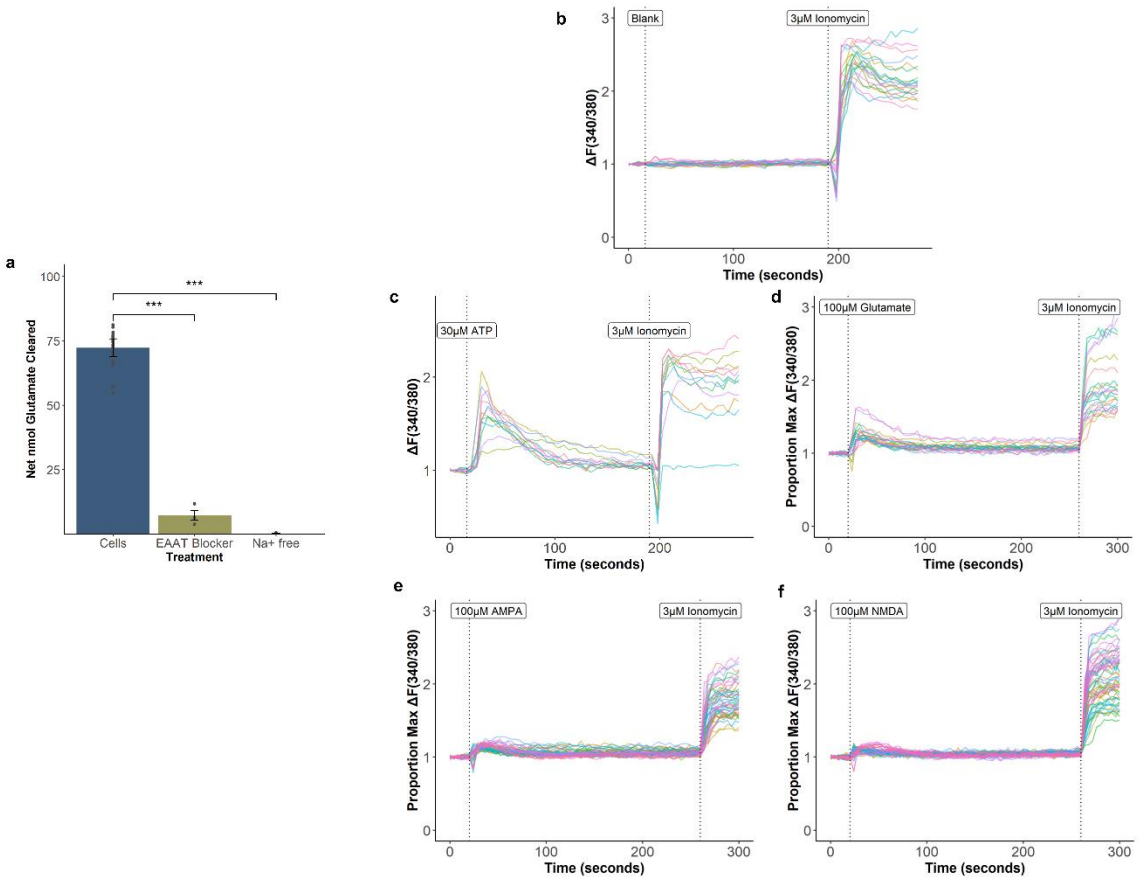

Supplementary Figure 11: Further validation of cell model. (a) Glutamate clearance of iAsts over 120-minute period. EAAT blocker DL-TBOA, NA^+ free, HBSS, NaCl replaced with equimolar choline chloride. Each point indicates an individual well experiment.DL-Bars indicate means ± 1 SD.***P<0.001 (ANOVA). **(b-f)** Flexstation time-response plots showing 340/380 emission ratio in response to various agonists. Plots were normalised to the mean of the first three recordings prior to addition of first agonist. Each line indicates the response of an individual well. N=3 biological replicates, each with two technical replicates.

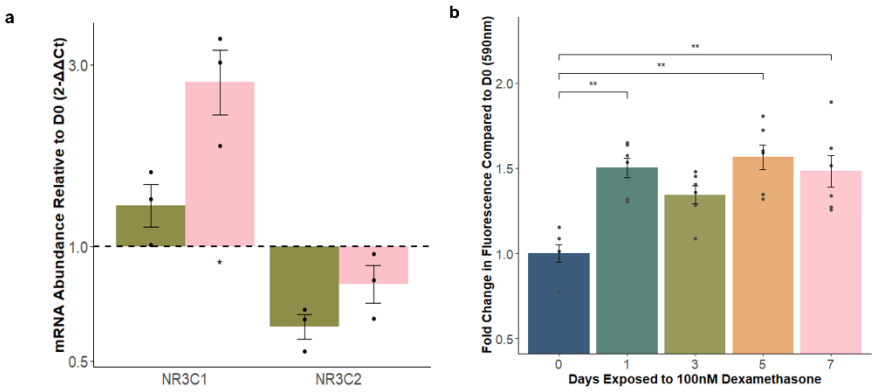

Supplementary Figure 12: Additional validation of stress paradigm. (a) qPCR of glucocorticoid receptors in response to 100nM dexamethasone. Significance relative to vehicle. **(b)** Presto blue assay to measure cell viability. Bars indicate mean ± SD. Each point represents and individual well. N=3 biological replicates, each with two technical replicates. *P<0.05, **P<0.01 (ANOVA, TukeyHSD).

Supplementary Table 1: Antibody information for antibodies used. Abbreviations: ICC, immunocytochemistry; IHC, immunohistochemistry

Antibody Target	Catalogue #	Company	Dilution	Species
EAAT2	ab41621	Abcam	IHC: 1:200 WB: 1:5000	Rabbit
SOX9	ab76997	Abcam	IHC: 1:200 ICC: 1:500	Mouse
AGT	AF3156	R&D Systems	ICC: 1:200	Goat
EAAT1	ab416	Abcam	ICC: 1:200	Rabbit
GS	GTX109121	GeneTex	ICC: 1:500	Rabbit
GFAP	AB5541	Merck Millipore	ICC: 1:1000	Chicken
FKBP5	sc-271547	Santa Cruz	ICC: 1:100	Mouse
GAT3	ab431	Abcam	ICC: 1:200	Rabbit
ALDH1L1	GTX84892	GeneTex	ICC: 1:100	Mouse
S100B	Ab52642	Abcam	ICC: 1:100	Rabbit
NESTIN	ABD69	Merck Millipore	ICC: 1:500	Rabbit
PAX6	AB_528427	DSHB	ICC:1:50	Mouse
OCT4	Ab18557	Abcam	ICC: 1:200	Mouse
NANOG	Ab21624	Abcam	ICC: 1:1000	Rabbit